

Novel Applications of Scanning Electrochemical Microscopy

by

David M. Roach

Thesis submitted to the Faculty of the Virginia Polytechnic Institute and State University
in partial fulfillment of the requirements for the degree of

Masters of Science
in
Chemistry

Mark R. Anderson, Chair
James M. Tanko
Gary L. Long

November 18, 2005

Blacksburg, Virginia

Keywords: Scanning Electrochemical Microscopy, Capillary Electrophoresis, Self-Assembled Monolayers, Site Selective Desorption, Lithography

Copyright 2005, David M. Roach

Novel Applications of Scanning Electrochemical Microscopy

by

David M. Roach

ABSTRACT

Scanning Electrochemical Microscopy (SECM) is most commonly used to spatially resolve reaction rates, image surface topography and surface reactivity. In this research, SECM is applied to various chemical systems in order to resolve local reaction chemistry and to produce patterns with dimensions of tens of microns in n-alkanethiol passivated gold substrates. Upon completing construction of the instrumentation, SECM was applied to capillary electrophoresis to accurately and reproducibly place the electrode directly above a very small capillary opening. Feedback SECM was then used to image and pattern surfaces, effectively distinguishing between insulating and conductive domains. Finally, the size of desorbed features patterned on a passivated gold substrate were studied as a function of both applied potential and ionic strength.

Electrochemical detection in capillary electrophoresis requires decoupling the voltage applied to the working electrode from the separation voltage applied across the capillary. End-capillary electrochemical detection achieves this by placing the electrode just outside the ground end of the separation capillary. Obtaining adequate signal-to-noise in this arrangement requires using small inner diameter capillaries. Decreasing the inner diameter of the separation capillary, however, increases the difficulty of aligning the microelectrode with the open end of the capillary. Using SECM, the position of the

capillary opening is determined while electroactive material is continuously emerging from the end of the capillary. The SECM instrument is then used to place the electrode at the position of maximum current for subsequent separations. Subsequent measurements found that the best signal-to-noise is obtained when the detection electrode is placed directly opposite the capillary opening and just outside of the capillary opening. When the electrode is further above the opening (but still opposite the capillary opening), the signal-to-noise does not dramatically decrease until the electrode is more than 30 μm above the 10 μm inner-diameter capillary. Limits of detection for 2,3-dihydroxybenzoic acid were found to be 8.2 fmol when aligned manually, and 3.8 fmol when the SECM is used to automatically align the microelectrode.

SECM was then used to image a series of multi-disk electrode arrays in order to demonstrate the ability of the instrument to discriminate between conductive and insulating domains. Upon demonstrating the capacity of the SECM to image very small domains of conductor on an insulating substrate, n-alkanethiol passivated gold surfaces were patterned using site-selective desorption. A number patterns, potentially useful for enzyme deposition, were subsequently produced in the passivated gold substrate. The feature size of the desorbed domains was monitored as a function of applied potential and the ionic strength of the solution used for desorption. Results showed that applying a more negative potential or increasing the ionic strength of the solution increased the magnitude of the electric field at the surface of the passivated gold substrate and resulted in a more complete, larger desorption. Both ionic strength and applied desorption potential prove to be parameters useful for controlling the size of patterned features in site selective desorption.

In Loving Memory of My Father

Richard Keith Roach

Acknowledgements

Paul McCartney and John Lennon once wrote, “I get by with a little help from my friends.” Never has this statement been more applicable than it has been in my tenure at Virginia Tech. No one has helped me more in my education and personal journey through college than my advisor, Mark Anderson. Mark is an exceptional man, a great advisor, and unlike others I have encountered in my time--Mark always believed in me. He has been supportive of me in good times and bad, and for that I will be eternally grateful. I am privileged to have worked with Mark and I am proud to call him my friend.

My committee, composed of Dr. Tanko and Dr. Long, I thank as well for all of their help in my education at Virginia Tech. Dr. Tanko has taught me much about chemistry and helped me in many facets of my research, while Dr. Long has helped me much in my tenure as a lab instructor. I would also like to thank Tom Wertalik for his help with the construction of all of the specialty glassware used in this manuscript. Tom is a skilled artisan, a good friend, and his help in the glass shop is most appreciated.

My family and friends have all been supportive of me during my stay at Virginia Tech and would like to thank them all for caring. My friends Brandon Martin, Lloyd Mayberry, and Chris Mays have all been there to make me laugh when I was down and lessen my worries when I was stressed out. I want to thank my family for always being there for me. Becky, Tom, Jason, Maggie, Katie, Lisa, Sharon, Leo, and Grandma—thank you. Mom, I love you most of all and I hope you know that without you, your help, and your guidance—I would be lost.

Finally, though he will never get to read this, I want to thank my dad. My dad was a smart, selfless, and good man. I miss him everyday. I often wonder, “Do I make you proud, dad?” I certainly hope the answer is yes.

Table of Contents

Chapter 1: Introduction to Scanning Probe Microscopy	1
1.1 Introduction to SPM.....	1
1.2 STM Description.....	2
1.3 Surface Imaging and Applications of STM	5
1.4 Limitations of STM	7
1.5 AFM: Initial Construction and Theory	8
1.6 The Modern AFM and Imaging.....	10
1.7 UME Review	13
1.8 SECM Description.....	15
1.9 Applications of SECM and Imaging of Biological Systems	17
1.10 Surface Patterning in SECM.....	20
1.11 Manuscript Overview	22
Chapter 2: Overview of Electrode Alignment Optimization in Capillary	
Electrophoresis Using a Scanning Electrochemical Microscope	25
2.1 Electrochemical Detection in Capillary Electrophoresis	25
2.2 Experimental Approach for Optimization of Electrode Alignment in Capillary....	28
2.3 Scanning Electrochemical Microscopy: Construction of a Versatile Scanning Electrochemical Microscope.....	31
2.4 Electrochemical Measurements	33
Chapter 3: Optimization of Electrode Alignment in Capillary Electrophoresis Using a Scanning Electrochemical Microscope Results and Discussion.....	36
3.1 Imaging Dopamine Eluting from a 20 μm Capillary	36
3.2 Imaging 2, 3-dihydroxybenzoic Acid Eluting from Separation Capillaries	38

3.3 Limits of Detection for Manual UME Alignment versus SECM UME Alignment	42
3.4 Summary	45
Chapter 4: Scanning Electrochemical Microscopy on Gold: Surface Imaging	47
4.1 Principles of Surface Imaging via SECM	47
4.2 SECM Imaging of MDEA Surfaces	50
Chapter 5: Scanning Electrochemical Microscopy of Modified Gold Surfaces:	
Surface Patterning and Manipulation	53
5.1 Patterning Gold Substrates via Molecular Self-Assembly and Site Selective Desorption: An Introduction	53
5.2 Imaging Gold Substrates Patterned via Selective Desorption	56
5.3 Experimental Approach for Surface Patterning and Manipulation	57
5.4 Site-Selective Desorptions Via SECM: Pattern Generation	59
Chapter 6: Controlling Desorbed Feature Size on a Modified Gold Substrate	63
6.1 Feature Size as a Function of Potential	63
6.2 Feature Size as a Function of Ionic Strength	67
6.3 Summary	70
Chapter 7: Summary and Future Work	72
7.1 Project Summary	72
7.2 Future Work	73
References	76

List of Figures

- Figure 1. (a) The STM tip is positioned by three piezoelectric elements that are subsequently used to scan the tip over the substrate surface. (b) The gray shading represents electron distributions around individual atoms and the black shading illustrates tunneling due to overlap of the electronic wave functions of the tip and the substrate..... 3
- Figure 2. STM false color image of the face centered cubic structure of nickel 110. The raised portions of the image represent individual nickel atoms¹¹..... 6
- Figure 3. Intermolecular potential energy curve demonstrating that at long ranges attractive van der Waals forces dominate but at close range electronic and nuclear repulsions control the deflection of the AFM cantilever. 9
- Figure 4. A modern AFM apparatus uses an optical lever to measure the cantilever deflection and a segmented tube piezoelectric element to move the substrate relative to the AFM tip..... 11
- Figure 5. A typical cyclic voltammogram for a UME. Oxidation of a of 0.25 mM ferrocene carboxylic acid in water with 0.1 M KCl as supporting electrolyte exhibits an $i_{T,\infty} = 0.9$ nA for this carbon-fiber ultramicroelectrode..... 14
- Figure 6. Schematic of SECM Apparatus..... 15
- Figure 7. When the UME is held far from the substrate, hemispherical diffusion occurs and a steady-state current, $i_{T,\infty}$, is reached. When the electrode is moved close to an insulator, diffusion to the electrode surface is hindered and $i_{T,\infty}$ decreases. When the UME is held close to a conductive substrate, a catalytic current greater than $i_{T,\infty}$ is observed..... 17
- Figure 8. When the UME approaches the surface in the presence of the enzyme-specific reactant, S, the effective concentration of the electron mediator, R, increases due to enzyme catalysis. The result is a current enhancement at the UME..... 20
- Figure 9. A typical carbon fiber UME is constructed by aspirating a carbon fiber into a glass capillary and pulling the tip to a fine point. Electrical contact is established via a capacitive coupling with approximately 5 cm of Ni wire inserted into the capillary, which is backfilled with 4 M sodium acetate and 0.15 M NaCl..... 30
- Figure 10. The locally constructed SECM instrumentation consists of a Thorlabs Inc. XYZ platform equipped with Z600 series actuators. The initial electrode position is established manually and then locally written software controls subsequent movement. A carbon fiber microelectrode is used as the SECM tip and all electrochemical measurements are conducted with an EG&G Princeton Applied Research Model 273A Potentiostat/Galvanostat. 31

Figure 11. This image illustrates a representative grid structure used to image electroactive compounds eluting from a capillary in CE. The initial grid of 1000 μm x 1000 μm and the smaller subsequent grids allow for both a large area to be imaged and high resolution near the area of highest current..... 33

Figure 12. Cyclic voltammetry was performed on 3 mM dopamine and 2,3-dihydroxybenzoic acid in 50 mM phosphate buffer (pH 6.8) at a scan rate of 100 mV/s.34

Figure 13. SECM image of dopamine emerging from a 20 μm capillary. A 0.010 M dopamine/phosphate buffer solution is continuously flowing through the capillary under the influence of a 15 kV potential applied across the length of the 60 cm capillary with a linear flow rate of 2.6×10^{-3} m/s..... 37

Figure 14. Image of 2,3-Dihydroxybenzoic acid as it emerges from the end of a 20 μm capillary. A 0.020 M 2,3-dihydroxybenzoic acid/phosphate buffer solution is continuously flowing through the capillary under the influence of a 15 kV potential applied across the length of the 60 cm capillary with a linear flow rate of 1.7×10^{-3} 38

Figure 15. Image of 2,3-dihydroxybenzoic acid as it emerges from a 10 μm capillary. A 0.020 M 2,3-dihydroxybenzoic acid/phosphate buffer solution is continuously flowing through the capillary under the influence of a 15 kV potential applied across the length of the 60 cm capillary at a linear flow rate of 1.7×10^{-3} m/s..... 40

Figure 16. Comparison of multiple injections of varying amounts of 2,3-dihydroxybenzoic acid detected by square-wave electrochemical detection when the microelectrode is aligned manually (B) and then aligned by the SECM (A). For each alignment, a series of 3 injections of 5 different amounts of 2,3-dihydroxybenzoic acid (260 fmole, 180 fmole, 130 fmole, 79 fmole, and 26 fmole) are introduced to the capillary using 5 second electrokinetic injections. 43

Figure 17. The calibration curves generated from electropherograms in Figure 15 establish the LOD for detection of 2, 3-dihydroxybenzoic acid for both a SECM aligned UME and a manually aligned UME..... 44

Figure 18. Approach curves generated by moving a 10 μm diameter Pt UME at 600 mV vs. Ag/AgCl close to a surface in a solution of 5 mM $\text{K}_4\text{Fe}(\text{CN})_6$ and 0.1 M KCl. When the tip approaches a conductor (A) feedback current is observed from the substrate; however, when the tip approaches an insulator (B) diffusion to the UME tip is hindered and the current decreases. 48

Figure 19. A wireframe SECM image of a 460 x 500 μm section of a MDEA shows peaks that illustrate the 100 μm diameter disks and the valleys that illustrate the insulating material that separates the disks. Experimental conditions: 10 μm Pt UME at 600 mV vs. Ag/AgCl, 5 mM $\text{K}_4\text{Fe}(\text{CN})_6$, and 0.1 M KCl..... 50

Figure 20. A wireframe SECM image of a 200 x 200 μm section of a multi-disk electrode array shows peaks that illustrate the 50 μm diameter disks and the valleys that illustrate the insulating material that separates the disks. The image was obtained using 5 mM $\text{K}_4\text{Fe}(\text{CN})_6$ and 0.1 M KCl as the mediator species and electrolyte species respectively in solution. The applied UME oxidation potential was 600 mV vs. Ag/AgCl. 51

Figure 21. A typical bulk reductive desorption of a decanethiol monolayer from a 2 mm gold substrate in aqueous 0.5 M KOH. 54

Figure 22. Schematic diagram of the SECM feedback imaging of the site specific desorption of the n-decanethiol monolayer. 56

Figure 23. SECM image of two 50 x 50 μm holes desorbed at -1.0 V vs. Ag/AgCl in a decanethiol modified gold substrate separated by 50 μm diagonally. The resulting image illustrates the desorbed holes are roughly twice the dimensions over which the UME tip is rastered. 59

Figure 24. SECM feedback image of a 150 x 150 μm island of decanethiol desorbed from a decanethiol modified gold substrate. The UME tip has been rastered about a 200 μm square resulting in a decanethiol island surrounded by bare gold. 60

Figure 25. SECM feedback images of a “VT” desorbed at -1.0 V vs. Ag/AgCl from a decanethiol modified gold substrate. A shaded relief map (top) shows one representation of the “VT”, while a more familiar false color image (bottom) shows the “VT” desorption from another perspective. All distances on the X and Y axes are in microns and the desorbed “VT” is approximately 200 μm tall and 400 μm long. 62

Figure 26. When a small potential is applied the electric field is localized to a small region between the UME tip and the substrate (A). If a larger potential is applied the area over which the electric field can affect the substrate is increased (B). 63

Figure 27. False color image of three lines desorbed from a decanethiol modified gold substrate. The desorption are at -1.1 , -1 , and -0.9 respectively from the top to the bottom vs. Ag/AgCl. Imaging conditions: 0.1 M KCl, 5 mM $\text{K}_4\text{Fe}(\text{CN})_6$, 20 mM KOH. 64

Figure 28. Two lines desorbed in a decanethiol modified gold substrate. The line desorbed at -1.0 V (pictured right) demonstrates a continuous desorption of thiol. The line desorbed at -0.9 V (pictured left) appears as two small desorbed holes in the monolayer. The patchy desorption at -0.9 V is consistent with the theory that desorptions are initiated at defect sites in the monolayer. 66

Figure 29. Three lines desorbed at ionic strengths of 0.05, 0.12, and 0.17 respectively from top to bottom using the same UME/substrate distance. A false color image of the desorptions (A) shows a map of the current as a function of distance while the shaded relief map (B) better illustrates the size of the desorbed holes in the decanethiol modified

gold surface. All distances labeled on the axes are in microns (desorption potential -1.0 V). 68

Figure 30. Cross section of three lines desorbed at ionic strengths of 0.07, 0.12, 0.17 from right to left. The increasing ionic strength increases effective electric field at the gold substrate. A larger applied electric field results in desorption lines of larger width and greater feedback response during SECM imaging..... 69

List of Tables

Table 1. Comparison of the peak current, baseline peak-peak noise, and baseline standard deviation as a function of electrode distance above the capillary opening obtained for a series of 5-second electrokinetic injections of 2 mM 2,3-dihydroxybenzoic acid.....	41
Table 2. Size of features and feedback current data for lines desorbed from a decanethiol modified gold substrate at different potentials.....	65

Chapter 1: Introduction to Scanning Probe Microscopy

1.1 Introduction to SPM

It is often said that “seeing is believing” and in keeping with this saying, scientists have developed telescopes that see deep into the heavens and optical microscopes that allow for magnification of minute objects. Microscopy is hundreds of years old dating back to Hooke who invented the light-optical microscope¹. Since Hooke, optical microscopy has been optimized to near perfection, such that only the fundamental laws of physics govern the maximum resolution that can be obtained by these microscopes (approximately 250 nm)².

In response to the resolution limits of the light-optical microscope, the first electron microscope was constructed in 1931³. The advantage of an electron beam microscope originates from the fact that the electrons exhibit a shorter wavelength than visible light, which translates into enhanced maximum resolution⁴. Two types of electron beam microscopes were developed. The transmission electron microscope (TEM) was pioneered first as it operates much like an optical microscope. Images in TEM are captured using a fluorescent screen². The scanning electron microscope (SEM) was developed shortly after the TEM and offered enhanced resolution. In SEM, the electron beam is focused onto a small spot and rastered over the surface of the analyte, while simultaneously electrons reflected from the surface are detected with an electron detector². These two techniques provided resolution enhancement over conventional optical microscopes, but were still limited by the quality of the lenses and the diffraction limit of the electron beam. Electron beam microscopy offers a significant resolution enhancement over optical microscopy as a skilled SEM operator can obtain images with a

resolution of approximately 10 nm on an ideal surface; however, atomic resolution with electron beam microscopy cannot be achieved necessitating the development of new techniques³.

Theory for the first scanning probe microscope (SPM) was described in 1972 by Ward, Young, and Scire⁵. Though their attempts to develop a working SPM were unsuccessful, they paved the way for G. Binnig to develop both scanning tunneling microscopy (STM) and atomic force microscopy (AFM)^{6,7}. These two techniques have become powerful tools for examining interfaces and are capable of atomic resolution. The theory and application of STM and AFM will be discussed at length along with another type of SPM, the scanning electrochemical microscope (SECM).

SECM is a powerful form of microscopy capable of imaging conductors, semiconductors, insulators, obtaining surface topography information, and imaging chemical events occurring at or near the electrode tip. SECM can be coupled with both AFM and STM and can provide information unattainable by either of these methods alone. Concordantly, the focus of this manuscript will be on all three of these forms of probe microscopy with an emphasis on SECM and its advantages, versatility, and its novel applicability to various chemical systems.

1.2 STM Description

Theory for scanning tunneling microscopy was described by Young, Ward and Scire almost a decade prior to the development of the working instrument⁵. Their theoretical explanation of the STM gave insight into tunneling of electrons between two conductors and described the construction of an instrument that could obtain high resolutions via tunneling current measurements. Binnig and Rohrer brought the theory

of an STM to fruition in 1982⁶ and won the Nobel Prize for their work in 1986. A schematic of the basic STM instrument constructed by Binnig and Rohrer can be seen in Figure 1.

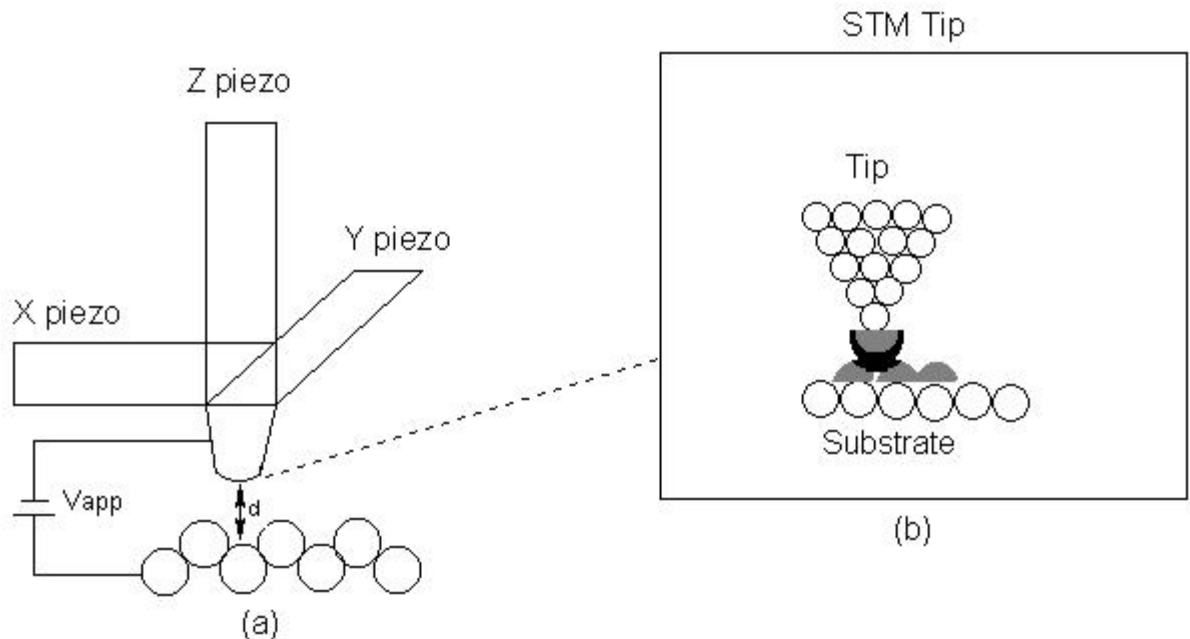


Figure 1. (a) The STM tip is positioned by three piezoelectric elements that are subsequently used to scan the tip over the substrate surface. (b) The gray shading represents electron distributions around individual atoms and the black shading illustrates tunneling due to overlap of the electronic wave functions of the tip and the substrate.

The theory of STM is fairly simple, yet the construction of the instrument is quite complex. The basic theory of STM involves bringing an atomically sharp tip towards a substrate surface (held at a bias potential relative to the tip) until the wave function of the atom at the electrode tip and the wave function of an atom from the substrate overlap. At this distance, quantum mechanical tunneling can occur and a measurable current (pA to nA) will begin to flow at the electrode tip. Quantum mechanical tunneling is a non-faradaic process so the flow of this current does not chemically alter the surface. The tunneling current measured between two conductors obeys the following expression^{2, 8}:

$$i_{\text{tun}} = I_0 * \exp(-A\sqrt{t}(\phi d)) = V_{\text{app}}/R_{\text{tun}} \quad (1)$$

where A is a constant equal to $1.025 \text{ eV}^{-1/2} \text{ \AA}$, ϕ is the barrier height, and d is the distance between the electrode tip and the substrate. The current obeys Ohm's law and thus is also equal to the tip-substrate bias, V_{app} , divided by the resistance to tunneling, R_{tun} , which varies with tip-substrate distance but is typically on the order of 10^9 to 10^{11} ohms⁸. The tunneling barrier for a typical STM analysis of a conducting surface is approximately 10 \AA^6 .

Examining the relationship in equation one, changing the distance, d , by just one angstrom can change the tunneling current an order of magnitude. The result of this relationship is an important one because it denotes that the majority of the tunneling current is carried by the atom at the very tip of the STM working electrode. As the resolution of any scanning probe microscopy is dependent on the size of the tip used to analyze the substrate, probe microscopy that uses a tip essentially one atom in size provides the highest resolution possible in SPM. The implications of equation one are also important in the aspect of tip construction. Construction of a STM working electrode tip that has one atom displaced 1 \AA from the bulk of the electrode tip is not difficult to realize.

Typical electrode tips in STM are constructed of either platinum/iridium or tungsten wires. Commercially available STM tips are available for purchase, but many labs produce their own tips in house. Platinum/iridium tips are cut to a fine point and microscopic asperities at the electrode tip serve as the active tip during tunneling. Tungsten wires are typically electrochemically etched to create an atomically sharp point that serves as the active tunneling tip⁹. In either case, as long as one atom is displaced

approximately one angstrom from the bulk, atomic resolution can be achieved for surface imaging.

Another implication of equation one is that STM (as well as all other SPMs) must be completely isolated from vibrations. Small vibrations of the substrate or the tip can lead to dramatic changes in current in STM and severely impair the resolution. STM and other forms of SPM can be isolated from vibrations in a number of ways, but the most common include: conducting measurements in a basement to isolate the measurement from natural building vibrations, isolating the instrument from mechanical vibrations via use of an air table or suspending the apparatus from vibration absorbing elastic cables, and isolating the instrument from acoustic vibrations by enclosing the instrument in a solid casing. By combining these methods to isolate the system from vibration, very small sub-angstrom distances can be maintained throughout the measurement and higher resolution images can be obtained.

1.3 Surface Imaging and Applications of STM

Imaging in STM is best performed in “constant current mode” in order to avoid a tip crash into the substrate⁶. In this mode, a tunneling current is established and the current is held constant during the X-Y scan by means of a feedback loop to the z piezo. Deflection of the z piezo is recorded as a function of X-Y position and an atomic topographic image of the surface can be obtained.

The plots made in STM are usually gray-scale or false color images, plots that can be quite striking as to their resolution of surface topography (Figure 2). Highly ordered pyrolytic graphite (HOPG) is the ideal STM surface as it is typically atomically smooth and an excellent conductor. Graphite has a layer structure whereby sheets of graphite

consisting of carbon in a honeycomb arrangement are stacked upon other sheets forming the solid structure. Atomically resolved images of HOPG via STM have provided information about the atomic ordering of the carbon atoms relative to one another. The distances between the carbon atoms in HPOG has been determined to be 2.46 Å and 1.42 Å with the adjacent layers being separated by a thickness of 3.35 Å¹⁰.

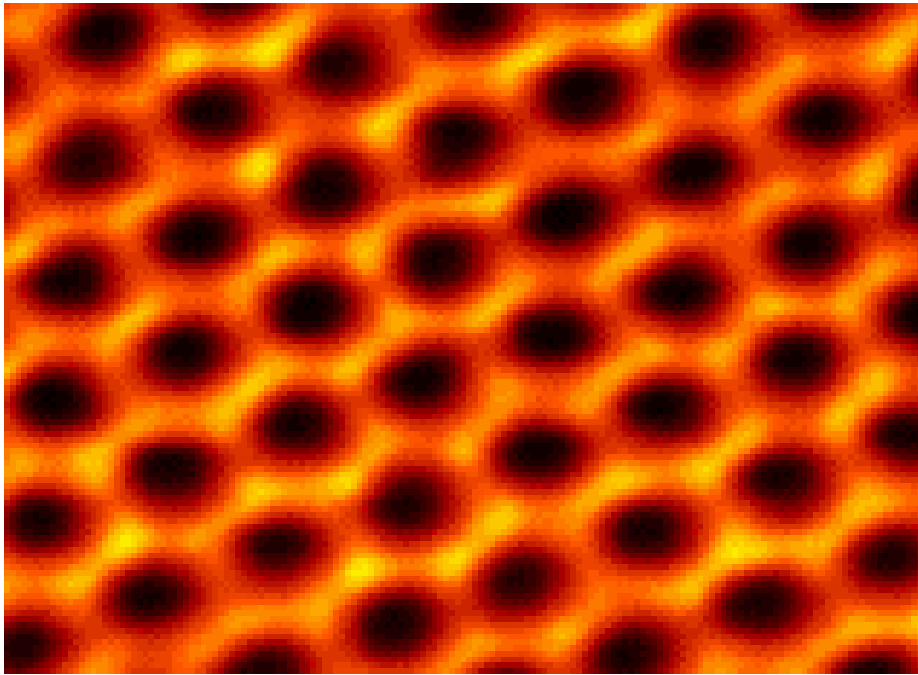


Figure 2. STM image of the honeycomb structure of HOPG. The dark portions of the image represent individual carbon atoms.

Imaging in STM has not only proven useful for gaining information about the packing of many conducting substrates, but can also provide information about adsorbates on these conducting surfaces⁸. Molecules that chemically adsorb to the surface of an electrode can also be imaged by STM, though the mechanism for electron tunneling for non-conducting adsorbates is not fully understood². Examples of adsorbate studies conducted using STM include iodine adsorption, and determination of the structure of self-assembled monolayers (SAMs) on various substrates. In a classic STM

study by Yau, Vitus, and Schardt, a platinum (111) substrate was examined by STM. An iodine layer was adsorbed to the Pt (111) surface and the resulting monolayer was found to assemble in a $\sqrt{3} \times \sqrt{3}R30$ pattern atop the platinum substrate¹¹. A similar study of adsorption of 4-aminothiophenol onto a gold (111) substrate was performed by Kim, McCarley, and Bard. The resulting STM images of the adsorbed layer exhibit different spacing than the gold (111) substrate and confirm the theorized $\sqrt{3} \times \sqrt{3}R30$ geometry for packing of these molecules on the surface¹².

1.4 Limitations of STM

It has been shown that STM can be used to image low-doped semiconductors¹³ and conductors with insulating monolayers adsorbed to the surface¹². Unfortunately, bulk insulators cannot be imaged with STM as no tunneling current is observed in these systems. Another limitation of STM is that it can only be used on atomically smooth substrates. As the tunneling barrier is a mere 10 Å, even minimally rough surfaces can cause the STM tip to crash into the substrate even when operating in constant current mode. An additional limitation is that STM studies are typically performed in vacuum. Some STM studies can be performed in air, and with sufficient supporting electrolyte some liquid state STM studies can be performed (though this requires a complex experimental setup)⁸. Due to experimental conditions required for STM, most surfaces are unable to be examined in their natural environment. It quickly became clear a new SPM was needed that could circumvent the limitations of STM and show greater applicability to non-ideal surfaces.

1.5 AFM: Initial Construction and Theory

In response to STM's inability to image insulators, the first atomic force microscope (AFM) was described by Binnig, Quate, and Gerber in 1986⁷. The first AFM was born as a merging of STM and a stylus profilometer (SP). A stylus profilometer consists of a sharp stylus tip attached to a cantilever beam that traverses a sample surface. This technique has reported resolutions of 1000 Å laterally and 10 Å vertically¹⁴. The limitation of SP is that a rough surface can be plastically deformed by the stylus as the forces on the stylus tip can be appreciable (10^{-2} to 10^{-5} N)⁷. The AFM described by Binnig et al. included a very sharp diamond tip attached to a gold cantilever that had a STM positioned above it to measure small deflections of the cantilever due to molecular forces between the tip and the substrate. The sample was attached to a three-dimensional piezoelectric drive capable of moving in the x, y, and z directions. The sample was moved relative to the AFM tip, unlike in STM where the sample is static and the STM tip is rastered above. The resulting images had resolutions of 30 Å laterally and approximately 1 Å vertically and did not damage the substrate surface⁷.

The substrate surface is not deformed in AFM because unlike SP, the tip is maintained a minute distance from the substrate surface. The cantilever deflection is a function of the separation-dependency force between two entities. These molecular forces include electrostatics, van der Waals forces, and at close range, nuclear and electronic repulsions. A typical AFM scan begins by generating a force curve to assess the extent of the molecular interactions between the tip and the substrate⁸. Initially the tip is positioned about 20 nm from the substrate surface where no molecular interactions occur and the cantilever is straight. The distance is decreased to about 10 nm where only

electrostatic attractive or repulsive forces take place. These forces cause a deflection in the cantilever and knowing the spring constant of the cantilever the electrostatic forces can be estimated. When the tip is then distanced less than 3 nm away, attractive van der Waals forces begin to contribute to the deflection of the cantilever toward the substrate. When the van der Waals forces become large compared to the spring constant of the cantilever times the existing deflection the tip will “jump to contact”. At contact, the nuclear and electronic repulsions begin to dominate and the overall potential energy of interaction becomes repulsive (Figure 3)¹⁵. Imaging is conducted in “contact” mode where the AFM tip is as close to the surface as possible and the forces are repulsive⁸.

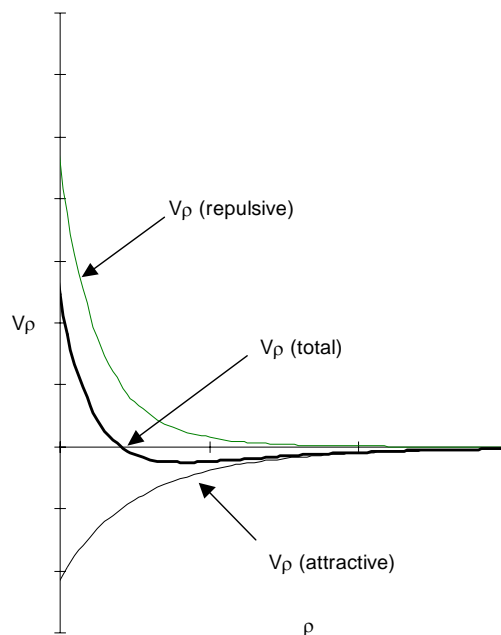


Figure 3. Intermolecular potential energy curve demonstrating that at long ranges attractive van der Waals forces dominate but at close range electronic and nuclear repulsions control the deflection of the AFM cantilever.

The reason the majority of AFM measurements are performed in the repulsive portion of the potential surface is that most AFM experiments are performed in air (though AFM can be performed in solution or vacuum). It has been shown that bringing a sharp tip near a planar surface in moist air generates spontaneous capillary

condensation of water vapor; the surface tension of the ensuing meniscus deflects the AFM tip to the substrate¹⁶. The onset of the capillary condensation brings about a rapid “jump to contact” with a surface force of 10^{-8} to 10^{-7} N¹⁷. This makes operation in the attractive portion of the potential energy curve difficult and dictates the tip-substrate distance must be small so that the repulsive interactions are strong enough to be measured. Due to the meniscus, these repulsions typically involve more than one atom, making atomic resolution with AFM in air unattainable¹⁷. Atomic resolution of ideal surfaces (including HOPG) using attractive-mode in vacuum, however, has been achieved¹⁸.

1.6 The Modern AFM and Imaging

The modern AFM is slightly different than the initial AFM constructed by Binnig (See Figure 4). The modern AFM uses an optical lever consisting of a laser source that is reflected off a mirror mounted on the cantilever. As the cantilever is deflected due to changes in surface topography, the laser beam is deflected by an amplified amount depending on the length of the optical lever. A segmented photodiode is used to measure the deflection of the laser beam as the cantilever traverses a surface¹⁹. The response from the photodiode is then input into a feedback controller that adjusts the z-axis of a segmented tube piezoelectric element (a piezo capable of moving a sample in three dimensions)²⁰. The laser deflection as a function of X-Y position is recorded on a computer and topographic plots of the surface can then be made. The cantilever tip in a modern AFM is typically pyramidal-shaped silicon nitride; however, other tips including chemically modified probes can be used to gain additional surface information².

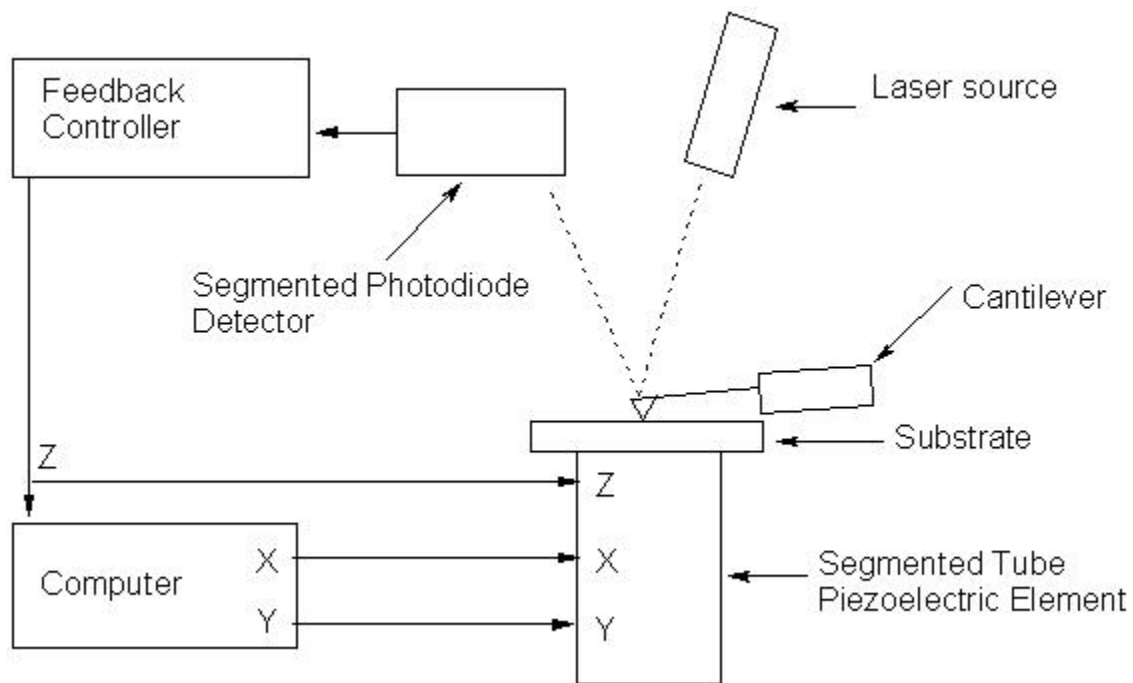


Figure 4. A modern AFM apparatus uses an optical lever to measure the cantilever deflection and a segmented tube piezoelectric element to move the substrate relative to the AFM tip.

In AFM, resolution and image quality is limited by a number of factors including tip shape, separation dependence of the force, specimen deformation, scanner imperfections, thermal drift, mechanical noise, and electronic noise². Despite all of these limiting factors, AFM can still attain atomic resolution in vacuum, and provide valuable surface information on a wide range of samples. AFM is applicable to conductors, insulators, biological samples, rough surfaces, and surfaces that are difficult to analyze in their natural environment using STM.

There are many different imaging modes in AFM but the two most prevalent modes are contact and tapping mode. Contact mode is merely scanning over the sample in the X-Y plane with the AFM tip held close to the substrate and measuring the cantilever deflection as previously described. Tapping mode AFM uses the same

apparatus; however, in this case, the cantilever is vibrated at a frequency of 50,000 to 500,000 hertz with an amplitude of about 200 Å¹⁷. Tip-substrate forces will decrease the vibrational amplitude of the tip and this amplitude dampening is input into the feedback controller to maintain the tip-substrate separation and generate topographic surface data. Tapping mode has a few advantages but one of the most exploited advantages is that it minimizes lateral forces exerted by the tip on the sample¹⁷. Tapping mode is commonly used to circumvent adhesion of the tip to the substrate surface in systems where this is a problem. Tapping mode can also be used to probe slightly below the surface in some instances. In a situation analogous to tapping along a wall and being able to differentiate between a stud and a hollow spot, tapping mode AFM can be used to observe solid nanoparticles buried below a thin surface film²¹.

Though AFM is a powerful surface topography analysis tool, it lacks the ability to image chemical reactions. Gold AFM tips have been modified with 11-mercaptoundecanoic acid to probe chemical interactions between a carboxylic acid and various organic functional groups on a surface in a technique called chemical force microscopy (CFM)²². While CFM imparts some chemical information about a surface, specifically frictional forces between various functional groups, the information obtained does not impart much mechanistic understanding of a given system. Another scanning probe technique is necessary to “see” reaction chemistry and gain chemical information about surfaces. The SPM of choice for gaining chemical knowledge about a surface is scanning electrochemical microscopy (SECM), a powerful technique that can reveal surface properties, topography, reaction chemistry, and kinetic data⁸.

1.7 UME Review

Understanding SECM and appreciation of the quantitative abilities of the measurements made with this device is dependent upon a comprehension of electrochemistry at ultramicroelectrodes. The behavior of ultramicroelectrodes has been the focus of a number of reviews^{23, 24}. An ultramicroelectrode (UME) is defined as an electrode having at least one dimension on the order of microns⁸. UMEs have many advantages, however, five major advantages of using UMEs render them very attractive for electrochemical analysis. UMEs can be used in systems of small dimensions where larger electrodes simply cannot fit. UMEs have a smaller surface area so the capacitive current associated with these electrodes is not as great, thus allowing for analysis of systems with faster kinetics. The smaller dimensions of UMEs allow the use of more resistive aqueous solutions. Disk UMEs are not subject to semi-infinite linear diffusion, rather they exhibit hemispherical diffusion—a situation that allows greater faradaic current to flow. Finally and most importantly to SECM, UMEs rapidly build up a diffusion layer of fixed length that is immune to convective effects such as solution stirring⁸.

When the diffusion layer becomes fixed, the current limits to a value that is completely controlled by the rate of mass transfer via diffusion of electroactive species from the bulk solution to the electrode surface²⁵. This limiting value is called the steady-state current and can be seen in the cyclic voltammogram shown in Figure 4. The value for the steady-state current at a disk UME of radius A in an insulating sheath is given by:

$$i_{T,\infty} = 4nFDC^*A \quad (2)$$

where n is the number of moles of electrons transferred, F is Faraday's constant, D is the diffusion coefficient of the electroactive species, and C^* is the bulk concentration of the electroactive species in solution.

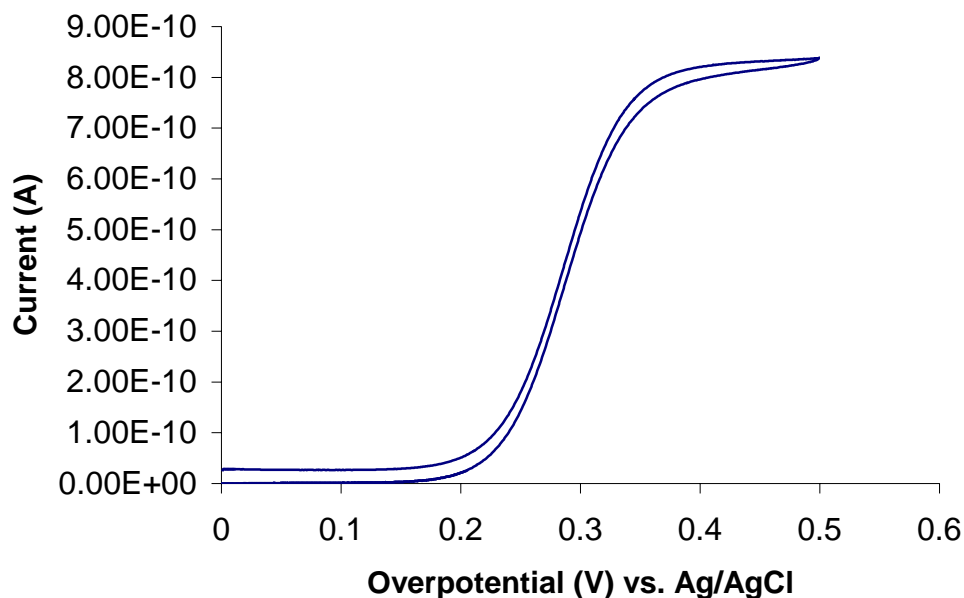


Figure 5. A typical cyclic voltammogram for a UME. Oxidation of a of 0.25 mM ferrocene carboxylic acid in water with 0.1 M KCl as supporting electrolyte exhibits an $i_{T,\infty} = 0.9$ nA for this carbon-fiber ultramicroelectrode.

The fixed diffusion length of a UME ultimately allows it to be scanned over a surface in SECM without convective effects disturbing the current observed. This is a desirable situation as topography and chemical information gained from a given system in SECM is ultimately determined by the current measured. Any aberration in this current causes resolution in SECM to suffer. Also as UMEs are characterized by their small currents, iR drops in solution during passage of current are insignificant²⁵.

1.8 SECM Description

SECM is typically performed using an apparatus similar to the block diagram shown in Figure 5. The substrate is held in an electrochemical cell containing a reference electrode, auxiliary electrode, solution with supporting electrolyte, and the sample substrate. The UME tip is moved in the x, y, and z directions using either mechanical inchworm actuators or piezoelectric elements. The potential bias of the electrode tip is controlled by a bipotentiostat that can also be used to apply a bias to the substrate. A computer is used to adjust the position of the UME, control the bipotentiostat, and record the observed current as a function of X-Y position.

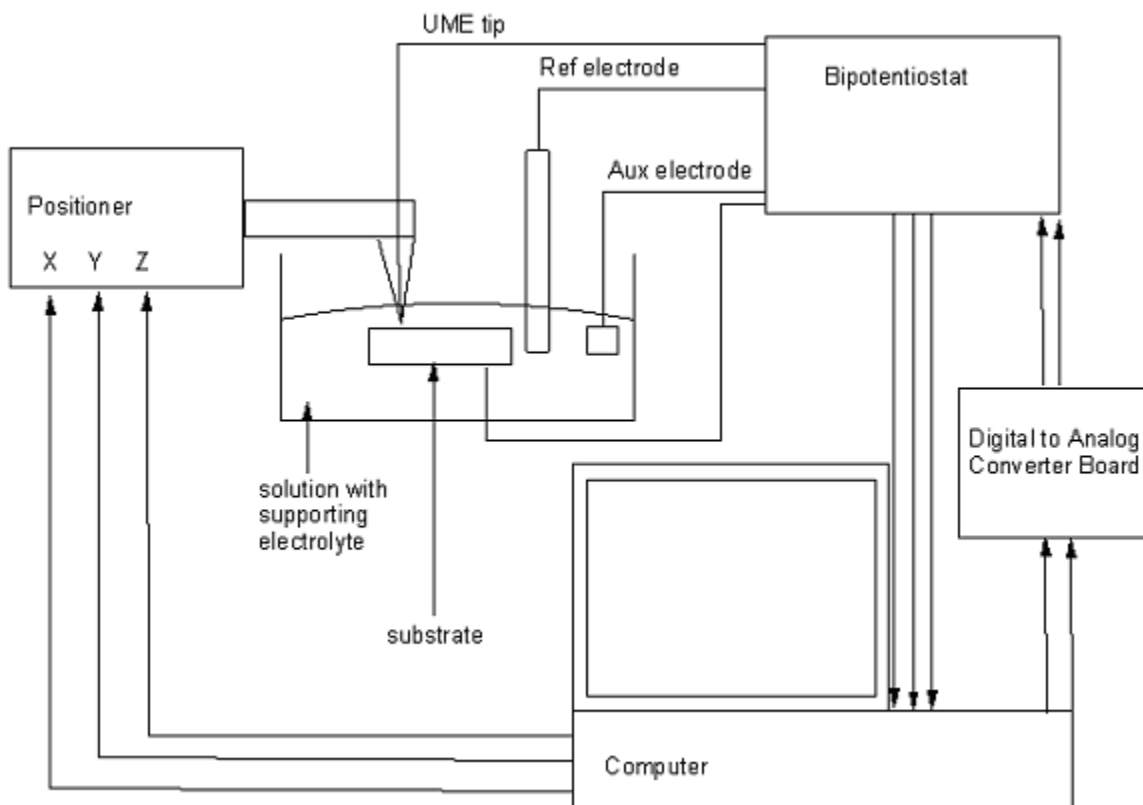


Figure 6. Schematic of SECM Apparatus.

The typical imaging operation mode of SECM is feedback mode, which is performed in the presence of a reversible redox couple. The basic principles of feedback

mode are illustrated in Figure 7. Under normal circumstances in solution, a UME exhibits hemispherical flux of electroactive species and establishes a diffusion layer of fixed length; however, when a UME is moved within a few tip diameters of a substrate the diffusion layer is perturbed. Once the UME travels to within a few tip diameters, the diffusion layer is “squeezed” between the substrate and the insulating sheath surrounding the UME conductor. Diffusion to the electrode surface is then hindered as the insulating sheath and the substrate surface block diffusion of electroactive species to the reactive electrode surface. When the UME is positioned above an insulator the steady-state current, i_T , is decreased^{8, 25-27}. The closer the UME tip is brought to the substrate surface the more pronounced the effect becomes, until the tip-substrate separation approaches zero at which point i_T also approaches zero. This decrease in current observed with decreasing tip-substrate separation is termed negative feedback. Over a conductor, negative feedback is not observed as different phenomena occur. When the UME tip approaches a conductor, diffusion is still hindered as before but the conducting substrate can reduce the newly oxidized species, O, back to its original oxidation state, R. Generation of R at the substrate surface increases the flux of R to the UME surface and the observed current is then greater than $i_{T,\infty}$ ^{8, 25-27}. This phenomenon is known as positive feedback. As the tip-substrate distance approaches zero above a conductor, efficiency of the re-reduction increases and the observed current will be enhanced significantly.

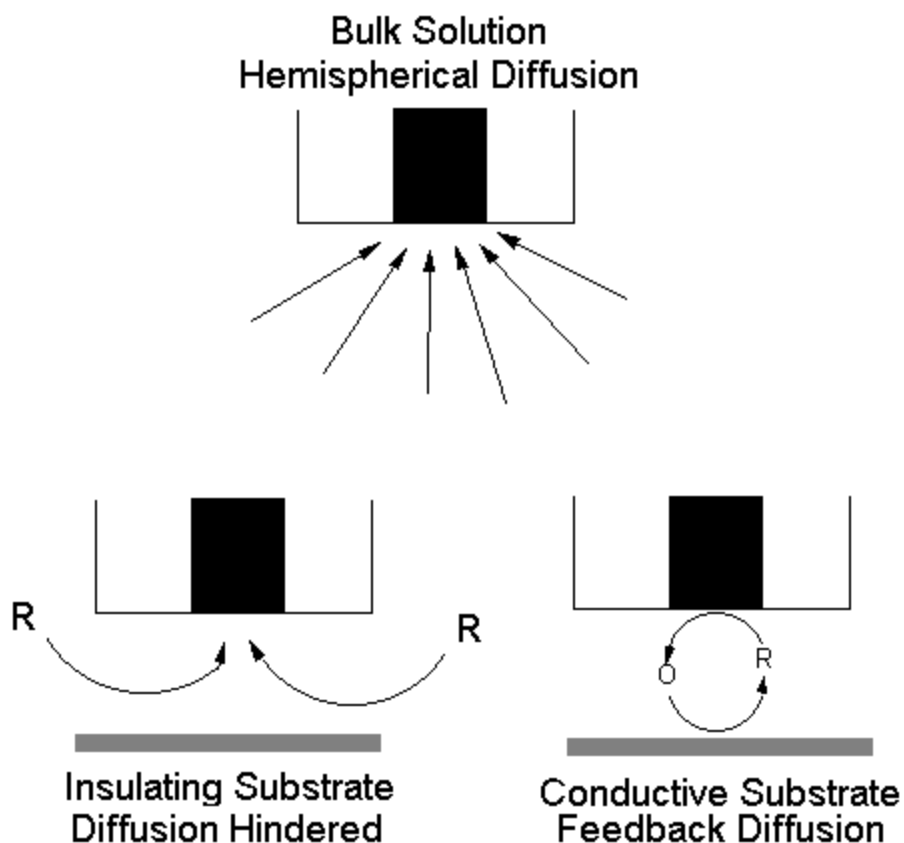


Figure 7. When the UME is held far from the substrate, hemispherical diffusion occurs and a steady-state current, $i_{T,\infty}$, is reached. When the electrode is moved close to an insulator, diffusion to the electrode surface is hindered and $i_{T,\infty}$ decreases. When the UME is held close to a conductive substrate, a catalytic current greater than $i_{T,\infty}$ is observed.

1.9 Applications of SECM and Imaging of Biological Systems

SECM is not just another electrochemical technique, but rather a different way of performing electrochemistry. Almost any type of electrochemical measurement (cyclic voltammetry, chronoamperometry, potentiometry, etc.) can be performed in an SECM setup. The unique ability of SECM to execute spatially-resolved electrochemistry greatly enhances the efficacy of commonly performed electrochemical techniques. The versatility of SECM allows it to be used in number of applications including topographic

imaging of surfaces, imaging of biological systems, UME shape characterization, heterogeneous kinetics measurements, homogeneous kinetics measurements, measuring ion and electron transfer processes between two immiscible liquids, examining ionic or molecular transport through membranes and thin films, patterning substrates, and monitoring surface reactions²⁵⁻²⁸. Though SECM has applicability to a wide range of systems, the two most relevant to the experimental work described in this manuscript are imaging (topographical and biological) and substrate patterning; ergo, the focus will be on these aspects of SECM operation.

Imaging in SECM is commonly performed in “constant height mode” where the UME tip is brought very close to the substrate surface and scanned in the X-Y plane without a feedback loop to the z-piezoelectric element. Operation in this mode requires a smooth, flat surface in order to avoid tip crashes into the substrate. SECM can produce topographic images of insulators, semiconductors, or conductors in this mode of operation. Plotting the X-Y position vs. the observed current at the electrode will produce a topographic plot of the substrate surface. The resolution of the resulting image is (as in all other SPM methods) governed by the size of the probe; in this case by the size of the UME used. SECM can be performed in “constant current mode”, analogous to that used in STM, but this method is used much less frequently. SECM not only exposes surface topography but can also differentiate between a conductor and an insulator on the surface as best demonstrated by imaging interdigitated electrode arrays²⁹.

While imaging surfaces in feedback mode of SECM is a very useful technique, one of the unique advantages SECM has over other SPM methods is that SECM has the ability to perform chemical imaging by spatially resolving differences in reaction rates at

varying locations in solution or on a substrate surface. This mode of SECM is particularly valuable for studying biological materials and surfaces that have chemically active and passive sites²⁹.

The ability of SECM to image topography and reaction chemistry has been applied to various biological systems including plant physiology. A leaf immersed in a solution of $\text{Fe}(\text{CN})_6^{4-}$ can be imaged by SECM and individual stoma can be seen in the surface topography³⁰. Furthermore, the SECM tip can be used to detect the opening of stomata in the presence of 0.1 M KCl and to detect oxygen release at the stomata upon illumination of the leaf in a solution saturated with carbon dioxide³¹.

SECM has also found applicability to artificially patterned biological systems³²⁻³⁴. Some enzymes can be immobilized locally at a substrate surface and products of the enzymatic reactions can be quantified directly or indirectly. Immobilizing glucose oxidase at a surface in the presence of a redox mediator and the enzyme specific reactant (β -D-glucose) results in an enhanced flux of the mediator, R, to the UME surface and thus a current enhancement (see Figure 8)³². Arrays of immobilized glucose oxidase spots on a substrate surface have recently been reported and enzyme activity at these enzyme spots has been characterized by SECM³⁵. As amperometric biosensors have recently become a very lucrative area of electrochemistry, the future of biosensor arrays and enzyme activity determination by SECM is certainly a bright one.

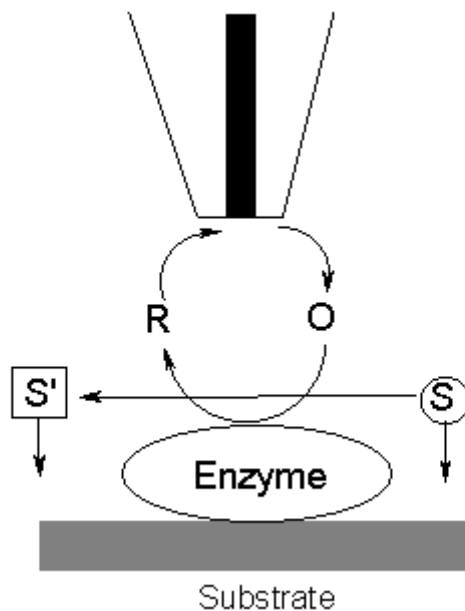


Figure 8. When the UME approaches the surface in the presence of the enzyme-specific reactant, S, the effective concentration of the electron mediator, R, increases due to enzyme catalysis. The result is a current enhancement at the UME.

1.10 Surface Patterning in SECM

When the UME is moved close to a substrate surface, electron transfer is confined to a small area on the surface²⁵. Upon realization of this property of the SECM, micropatterning of surfaces became a new area of study in electrochemistry. The direct mode of patterning a substrate is performed by approaching a conductive surface with a biased UME. The substrate functions as the auxiliary electrode, consequently, if a reduction takes place at the UME an oxidation must take place at the conducting substrate. As the entire substrate is biased, localization of this phenomenon on the substrate is caused by the distribution of the electric field between the UME and the substrate²⁵. To ensure localization to the greatest possible extent, the distance between the UME and the conductive surface must be kept as small as possible.

Recently, this method has been used by Schuhmann to generate patterns having micrometer dimensions on a gold substrate previously modified with a monolayer of an inert, passivating, n-alkanethiol^{36,37}. The method is based on the reductive desorption of alkanethiols from a gold surface³⁸. As negative potentials are applied to a gold substrate, the Au-S bond of the adsorbed alkanethiol is reduced in a one-electron process and the thiolate desorbs from the surface. If the reductive desorption is performed in an aqueous base (e.g. 0.5 M KOH), the desorbed thiolate diffuses away from the surface without the opportunity to re-adsorb to the newly exposed gold surface. It has been shown that this process completely removes the alkanethiol from the surface^{38,39}. This process is performed in SECM by using the UME as the auxiliary electrode and moving it as close to the gold surface as possible to localize the electric field. A negative potential is then applied to the gold substrate and desorption occurs in an area approximately equal to the size of the UME^{36,37}. By rastering the microelectrode over the surface of the gold, one can desorb the alkanethiol in whatever pattern one desires. The exposed gold can subsequently be modified by enzyme deposition as described by Schuhmann⁴⁰.

Another micropatterning technique that can be performed by SECM involves using Fenton's reaction (eq 3 and 4) to electrochemically generate hydroxyl radicals to modify a surface⁴¹.



These highly reactive radicals react with end-functional groups of adsorbed monolayers, altering their ability to adsorb or covalently attach an enzyme. Matsue modified a glass surface by adsorbing a layer of (3-aminopropyl)trimethoxysilane and deactivating parts

of the adsorbed monolayer via degradation of the amino end-group functionality by hydroxyl radicals. The UME is passed over the portion of the monolayer one desires to deactivate and trivalent iron is reduced to divalent iron in the presence of hydrogen peroxide. The result is the production of hydroxyl radicals that scavenge the surface local to the UME and deactivate the adsorbed monolayer at that position. A diphorase enzyme was then covalently attached through the amino groups of the remaining active sites using a glutardialdehyde as a cross-linking agent⁴¹. Biological surface spots were thus achieved by removing some of the reactive sites for enzyme deposition rather than creating new active sites for deposition.

1.11 Manuscript Overview

The unique ability of SECM to execute spatially-resolved electrochemistry greatly enhances the efficacy of commonly performed electrochemical techniques. The ability to pattern surfaces and spatially resolve differences in reaction rates at varying locations in solution or on a substrate surface opens a world of possibilities for the utility of such an instrument. The remainder of this manuscript will focus on the construction of a SECM, novel application of the SECM to image electroactive species eluting from small inner diameter capillaries in capillary zone electrophoresis (CZE), the advantages of UME alignment by SECM for subsequent CZE separations, simple surface imaging, surface modification, proof of concept for construction of a biosensor array, and surface patterning.

This manuscript will present the results of these studies in the following manner:

Chapter 2 will describe the difficulties associated with performing electrochemical detection in capillary electrophoresis and discuss the experimental details

for optimization of electrode alignment in capillary electrophoresis using a scanning electrochemical microscope. The goal of this chapter is to facilitate the understanding of problems associated with detection in CZE and describe the experimental setup that allows coupling of SECM and CZE.

Chapter 3 will discuss the results obtained by imaging electroactive material continuously eluting from a CZE capillary. The results demonstrate that even a slight misalignment of the UME above the capillary can result in a significantly lower analytical signal. This chapter also shows the capacity of the SECM to place an UME reproducibly and reliably above the capillary opening with minimal user intervention.

Chapter 4 describes the principles of imaging surfaces in SECM, and demonstrates the capacity of the SECM to resolve small conductive domains on an insulating substrate. The principles of feedback are discussed and approach curves above and insulator and a conductor are shown to illustrate these principles. MDEAs are imaged to show that the SECM can unambiguously discriminate between small conductive domains (50 μm in size) separated by 50 μm .

Chapter 5 has a broader focus and describes self assembled monolayers, reductive desorption, site selective desorption, the experimental details used for site selective desorption, and shows a number of patterns generated by site selective desorption of decanethiol from a modified gold substrate. Patterning of surfaces is described in detail in this chapter and desorbed patterns are imaged via feedback SECM and presented as false color images.

Chapter 6 describes the manipulation of the magnitude of the electric field during site selective desorption to control feature size. Applied potential and ionic strength are

adjusted to change the electric field about the modified gold substrate and control the size of the features patterned on to the surface. It is shown that applying a more negative potential or using a higher ionic strength solution during site selective desorption results in broader features and more complete removal of the mercaptan from the surface.

Chapter 7 summarizes all of the work presented in this manuscript and describes the future direction of this project.

Chapter 2: Overview of Electrode Alignment Optimization in Capillary Electrophoresis Using a Scanning Electrochemical Microscope

2.1 Electrochemical Detection in Capillary Electrophoresis

Amperometric electrochemical detection for capillary electrophoresis separations is a sensitive technique that has found widespread application⁴²⁻⁴⁶. Amperometric electrochemical detection exhibits sensitivity similar to laser induced fluorescence (LIF) but does not require analyte derivitization or expensive optics²⁰. Amperometric electrochemical detection while applicable to a wider range of compounds, also maintains a degree of selectivity and can discriminate against compounds that are either not electrochemically active or that have oxidation potentials greater than the applied overpotential. In addition, electrochemical detection for capillary separations is particularly attractive because the electrochemical detection can be conducted on low volumes with little loss of sensitivity^{47, 48}.

Despite the advantages that electrochemical detection affords, a few drawbacks emerge with this detection method. The large electric field from the electrophoresis separation interferes with the electrochemical detection and potentially limits electrochemical detection as a viable detection method for CE^{44, 49, 50}. To avoid this interference, the electrophoretic field is decoupled from the field associated with the electrochemical detector. This decoupling has been accomplished in several different manners. The first electrochemical detector used with capillary electrophoresis, reported by Wallingford, employed a porous glass joint to attach a capillary extension beyond the ground end of the separation capillary to achieve decoupling^{42, 46}. Here the ground electrode for the electrophoresis was placed at the porous glass joint and the electrode for the electrochemical detection was positioned at the end of the capillary extension. By

separating in space the electrophoretic field from the electrochemical detection in this manner, Wallingford *et al.* demonstrated that good signal-to-noise (S/N) could be achieved with electrochemical detection. Extending the capillary beyond that used in the CE separation, however, reduced the efficiency of the separation by introducing opportunities for band broadening in the capillary extension where no forces acting to separate the analyte zones exist.

The use of a glass joint is not without disadvantages. The porous glass is fragile and, unless perfect alignment of the capillary extension with the separation capillary is made, then band-broadening becomes even more significant^{49, 51, 52}. Other types of joints, including Nafion and cellulose acetate, were subsequently used to replace the porous glass to provide a more robust joint with all of the advantages of porous glass^{49, 51, 53}.

Ewing and coworkers first reported the use of end-capillary detection with CE^{54, 55}. Here, a microelectrode is aligned with the open, ground, end of the capillary. By placing the detector just outside the open end of the separation capillary, band broadening from the capillary extension is eliminated, improving the overall efficiency of the CE separation. End capillary detection, however, potentially has lower S/N because of the close proximity of the separation electric field to the detector field. As the current associated with the electrophoresis scales with the square of the capillary diameter, the use of small inner diameter capillaries make end-capillary electrochemical detection practical and obviated the need for the capillary extension^{46, 47, 56}.

Although eliminating the extension improves the separation efficiency by minimizing band broadening, end-capillary electrochemical detection presents a new set of experimental challenges, such as reproducibility and accuracy of electrode alignment,

which influence the S/N of the detection⁵⁷. This problem is even more prominent as the size of the capillary opening approaches that of the microelectrode because electrochemical detection sensitivity is dependent on electrode alignment with the capillary opening. Baldwin avoids this problem by using an electrode whose surface area is larger than the capillary opening in a wall-jet arrangement for detection⁵⁸. In this arrangement, perfect alignment of the detection electrode with the capillary opening is not required, and Baldwin shows that good sensitivity can be obtained. The signal-to-noise advantages of a microelectrode, however, are lost when the detection is conducted with a large area electrode. Spatially-resolved measurements when using a small diameter microelectrode in the vicinity of the capillary outlet were previously described by Matysik⁵⁹. When using a 25 μm microdisk electrode that was positioned manually above a 75 μm inner-diameter capillary, Matysik found that the limiting current changed by only 2% within $\pm 40 \mu\text{m}$ of the capillary center, and by only $\sim 5\%$ within $\pm 80 \mu\text{m}$ of the capillary center. Reproducible alignment directly opposite the capillary opening when using an optical microscope is difficult to achieve and represents a major limitation of end-capillary electrochemical detection for capillary electrophoresis^{47, 56, 57, 60}.

Matysik's results demonstrated that, when using a small diameter microelectrode for detection in electrophoresis, the detector current is a function of the placement of the electrode relative to the capillary opening. Reproducibility of measurements, therefore, relies on the ability to place the detection electrode consistently in the same location. Reproducible alignment directly opposite a small inner diameter capillary opening using an optical microscope is difficult and represents a major limitation of end-capillary electrochemical detection for capillary electrophoresis^{47, 56, 57, 60}. Here, Scanning

Electrochemical Microscopy is used to measure the solute concentration in the volume surrounding the end of the separation capillary, producing an image of the concentration of an electrochemically active compound as it elutes from the capillary. This provides a mechanism for accurately aligning the electrode with the separation capillary.

2.2 Experimental Approach for Optimization of Electrode Alignment in Capillary

Reagents

All solutions were prepared using 18M Ω deionized (DI) water (Barnstead Nanopure II). Dopamine (DA), 2,3-dihydroxybenzoic acid (DHBA), poly(diallyldimethylammonium chloride) 20% by weight in water (PDADMAC), 1, 3-phenylenediamine, sodium acetate, NaCl, KCl, Na₂HPO₄, NaH₂PO₄, and NaOH were used as obtained from Sigma-Aldrich. Shell Epon Resin 828 epoxy resin was used as received from Shell.

Capillary Electrophoresis

Fused-silica capillaries (60 cm), obtained from Polymicro Technologies (Phoenix, AZ), having an outer-diameter of 360 μ m and inner-diameters of either 20 or 10 μ m were used in these measurements. Conventional flow (unmodified) capillaries were prepared for use by flowing a solution of 0.1 M NaOH for 30 minutes through the capillary using 15 p.s.i. of hydrostatic pressure followed by flowing a phosphate buffer solution containing 0.05 M KCl, 0.01 M NaH₂PO₄, and 0.01 M Na₂HPO₄ for 30 minutes. A Spellman CZE 1000R power source was used to apply a potential across the capillaries during the electrophoresis experiments.

Electrode Preparation

Glass-enclosed P55 carbon-fiber disk electrodes were prepared as previously described⁵². Briefly, the fibers were aspirated into glass capillaries, and then the capillary is softened and pulled around the fiber using an in-lab constructed pipette puller. The glass/fiber interface was then sealed with epoxy⁵². After curing, the exposed carbon-fiber was cut flat against the glass and polished on a diamond polishing wheel to produce a disk-shaped electrode. Electrical contact was established through a capacitive coupling with a wire inserted into the open end of the electrode capillary, which was backfilled with an aqueous solution composed of 4 M sodium acetate and 0.15 M NaCl. The radius of the electrode is determined from the steady-state current in the voltammetry of a ferrocene solution. Typical electrodes were found to have a radius of $\sim 7 \mu\text{m}$. Figure 9 shows a typical electrode.

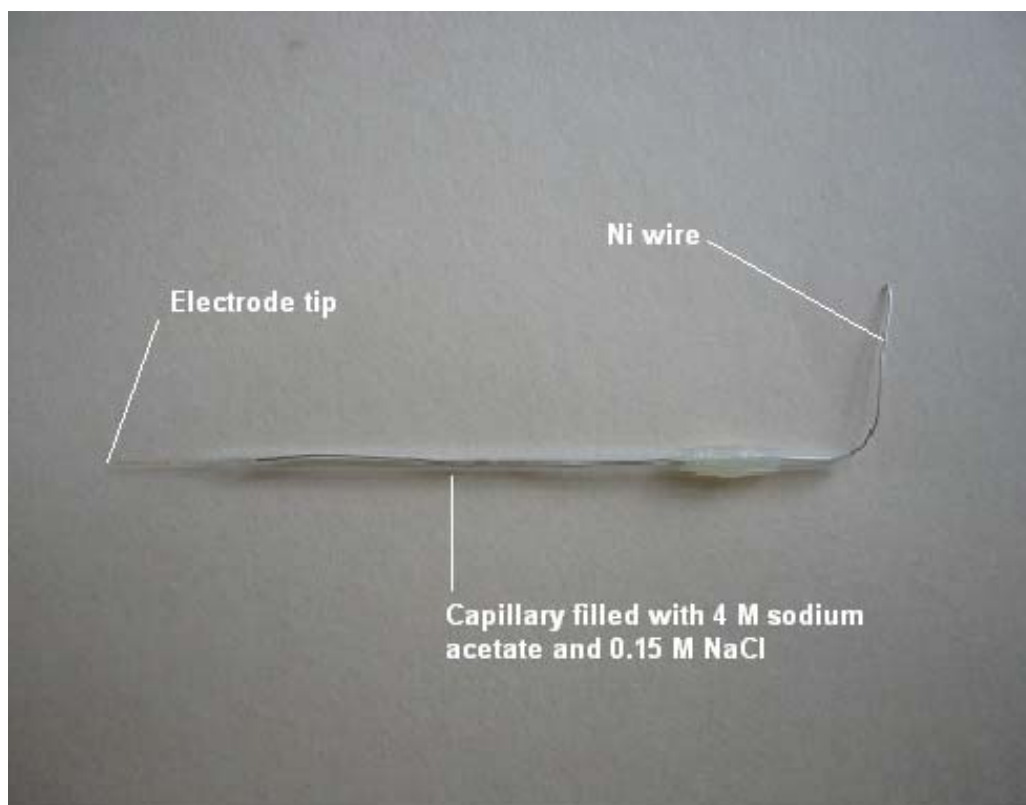


Figure 9. A typical carbon fiber UME is constructed by aspirating a carbon fiber into a glass capillary and pulling the tip to a fine point. Electrical contact is established via a capacitive coupling with approximately 5 cm of Ni wire inserted into the capillary, which is backfilled with 4 M sodium acetate and 0.15 M NaCl.

2.3 Scanning Electrochemical Microscopy: Construction of a Versatile Scanning Electrochemical Microscope

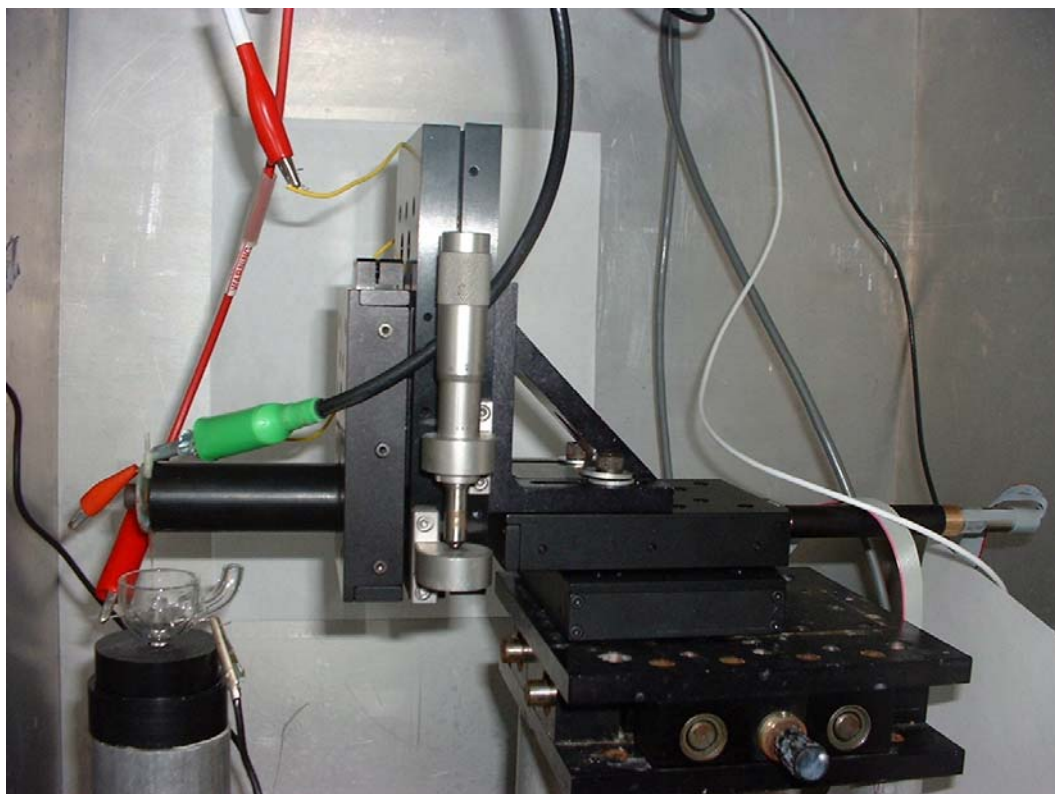


Figure 10. The locally constructed SECM instrumentation consists of a Thorlabs Inc. XYZ platform equipped with Z600 series actuators. The initial electrode position is established manually and then locally written software controls subsequent movement. A carbon fiber microelectrode is used as the SECM tip and all electrochemical measurements are conducted with an EG&G Princeton Applied Research Model 273A Potentiostat/Galvanostat.

The SECM instrumentation was constructed locally using a Thorlabs Inc. (Newton, NJ) XYZ platform equipped with Z600 series actuators operated in a closed loop configuration. The SECM apparatus is isolated from vibration by a TMC tabletop isolation platform (Technical Manufacturing Corporation, Peabody, MA). The working instrument can be seen in Figure 9. The initial X, Y, and Z position of the microelectrode relative to the opening of the electrophoresis capillary was established manually under

observation of a Leica GZ6E stereomicroscope. The actuators were controlled during the scanning electrochemical microscopy with locally written Software Visual Basic software. Step resolution for this instrumentation is 40 nm. The electrode potential for these measurements was controlled by an EG&G Princeton Applied Research Model 273A Potentiostat/Galvanostat (Oak Ridge, TN). The applied potential is referenced to an Ag-AgCl reference electrode.

When using the SECM to image the capillary opening during CE, a series of grids are monitored while maintaining the microelectrode at constant height (approximately 20 μm) over the end of the capillary. When acquiring the SECM data, the current is measured at each X-Y location and then the SECM moves the electrode to a new location. Each subsequent grid has increasing X-Y resolution, allowing increasing X-Y accuracy when determining the position where the maximum current is obtained. To achieve this, during each image-scan, the X-Y position with the maximum measured current is determined; and, then, a smaller area X-Y grid is initiated near this point. Initially, a 1 mm x 1 mm grid is scanned in steps of 100 microns to locate the elution zone of the capillary. The UME is repositioned near the point of the maximum and grids of smaller step sizes are scanned until an X-Y grid using steps that are 5 μm in length is used to image a 50 μm x 50 μm grid. The post map in Figure 11 illustrates the grid pattern that is used to locate the position of maximum current and auto align the UME above the capillary opening.

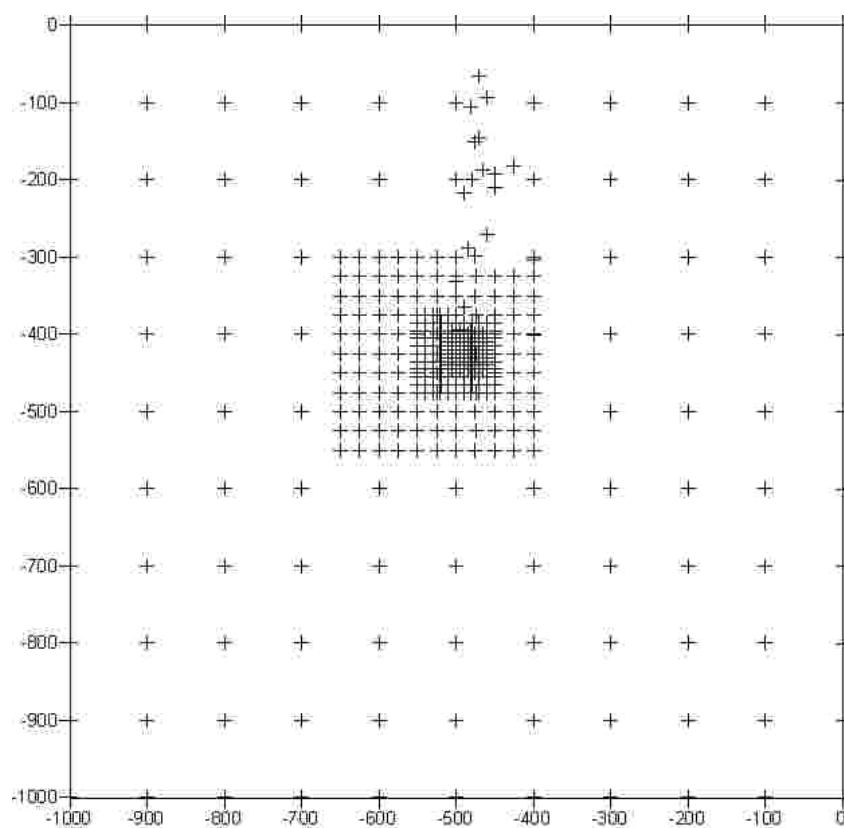


Figure 11. This image illustrates a representative grid structure used to image electroactive compounds eluting from a capillary in CE. The initial grid of 1000 μm x 1000 μm and the smaller subsequent grids allow for both a large area to be imaged and high resolution near the area of highest current.

2.4 Electrochemical Measurements

The cell for the electrochemical detector has been described previously⁶¹. Briefly, the separation capillary enters the electrochemical cell through a septum in the bottom of the cell, passes through narrow bore (500 μm) glass tubing, and the vertically aligned capillary then opens into a large (10 mL) reservoir that contains the CE buffer. The microelectrode is positioned above the opening of the capillary. The electrode potential

for these measurements was controlled by an EG&G Princeton Applied Research Model 273A Potentiostat/Galvanostat (Oak Ridge, TN).

The applied potential was chosen by performing cyclic voltammetry on both dopamine and 2, 3-dihydroxybenzoic acid to establish their respective oxidation potentials (Figure 12). Cyclic voltammetry showed that the oxidation peak potentials occurred at 220 mV and 360 mV for dopamine and 2, 3-dihydroxybenzoic acid respectively. During electrophoresis, the large applied separation voltage often brings about a positive shift in the observed half wave potentials for eluting analytes, thus, a larger applied potential is necessary to achieve a steady-state response⁵⁰. An overpotential of 650 mV was chosen for both dopamine and 2, 3-dihydroxybenzoic acid as both compounds gave a steady-state response at this overpotential with an applied separation voltage of 15 kV. All applied electrochemical potentials were referenced to an Ag-AgCl reference electrode.

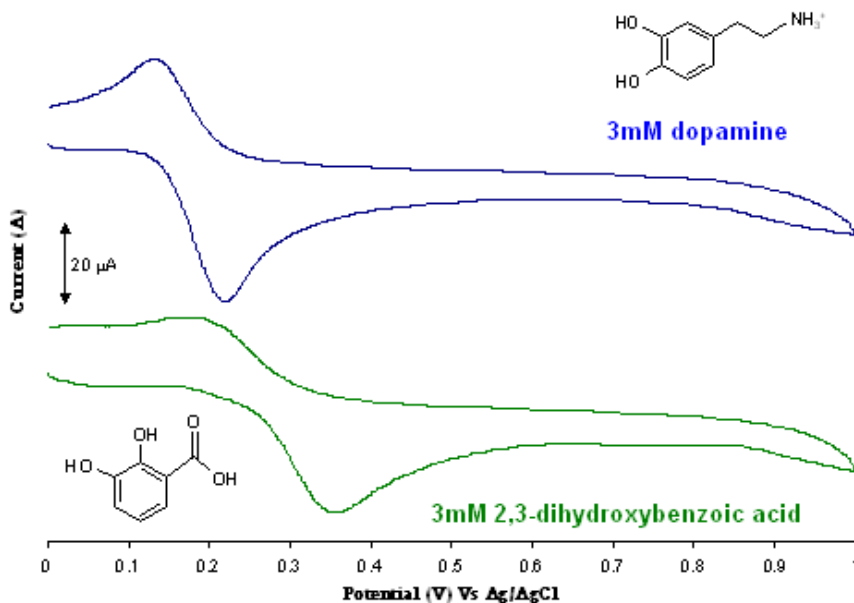


Figure 12. Cyclic voltammetry was performed on 3 mM dopamine and 2,3-dihydroxybenzoic acid in 50 mM phosphate buffer (pH 6.8) at a scan rate of 100 mV/s.

Carbon-fiber microelectrodes are initially positioned manually in the X, Y, and Z directions under observation with an optical stereomicroscope. Positioning of the electrode on the Z-axis, above the capillary, is accomplished by manually moving the electrode (under observation of a stereomicroscope) until it contacts the end of the capillary. This is indicated by a significant increase in the electrophoretic current due to the increased resistance along the separation capillary that occurs when the ground end is partially blocked by the electrode. The electrode is then moved 20 μm away from the capillary end. The lateral electrode placement is then optimized under the control of the SECM instrument. During the SECM determination, the potential of the carbon fiber is held at a constant value.

A fused-silica capillary (60 cm long) that has one end placed inside a plexiglass interlock-box and the ground end inside a Faraday cage containing an electrochemical cell and the SECM instrumentation is used for these measurements. The entire apparatus is isolated from vibration by a TMC tabletop isolation platform (Technical Manufacturing Corporation, Peabody, MA). The capillary ends are immersed in phosphate buffer and a potential difference of 15 kV is applied across the capillary. For SECM imaging, after a ten-minute stabilization period, a 0.020 M solution of an electroactive material in the phosphate buffer was introduced to the capillary under the influence of electrophoretic and electrokinetic forces. Flow of the electroactive compound was continuous during acquisition of the SECM image.

Chapter 3: Optimization of Electrode Alignment in Capillary Electrophoresis Using a Scanning Electrochemical Microscope Results and Discussion

3.1 Imaging Dopamine Eluting from a 20 μm Capillary

When using the SECM to automatically align a UME above a capillary, an electroactive compound moves through the capillary under the influence of the electrophoretic field until it emerges from the capillary opening and enters a 10 mL volume of background electrolyte. Electroactive material is imaged via SECM as it continuously emerges from the end of the capillary. As electroactive material constantly emerges from the capillary into the 10 mL volume of background electrolyte, the SECM data is collected as quickly as possible so not to allow a significant build-up of the bulk concentration of the electroactive material in the reservoir during the measurement (as the total volume of the separation capillary is very small, the amount of electroactive material introduced to the 10 mL reservoir during the time scale of a typical experiment is negligible.). This is accomplished by collecting data in a series of 10-step x 10-step X-Y grids, with each subsequent grid having smaller step sizes. By collecting data in this fashion, an area that is 1 mm x 1 mm can be imaged in approximately 10 minutes. An image of the concentration of dopamine as it emerges from a 20 μm inner diameter capillary is shown in Figure 13. Although the capillary opening is only 20 μm in diameter, measurable dopamine concentrations are found extending out approximately 400 μm in all directions from the position of the peak current. This is due to the continuous flow of dopamine through the capillary opening into the ground/detector reservoir. A concentration gradient surrounding the capillary opening results as the dopamine flows out of the opening and mixes with the bulk solution. The concentration

of the dopamine in these experiments will be highest directly opposite the capillary opening. Examination of a cross-section of the SECM data shows that the current decreases 10% from the maximum value within $\sim 30 \mu\text{m}$, and it decreases 25% from the maximum value within $\sim 120 \mu\text{m}$. This result is consistent with the report by Lu *et al.* and suggests that analyte zones can be detected even if the detection electrode is not perfectly aligned with the capillary opening⁵⁷. Poor alignment, however, will result in smaller peaks during the separation and lower S/N.

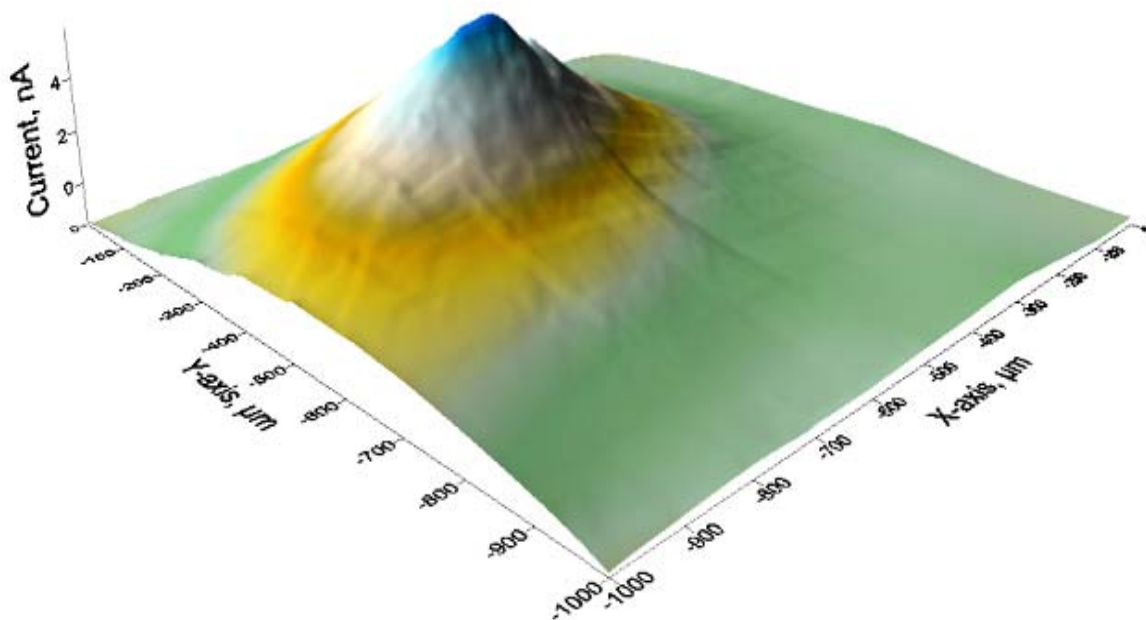


Figure 13. SECM image of dopamine emerging from a $20 \mu\text{m}$ capillary. A 0.010 M dopamine/phosphate buffer solution is continuously flowing through the capillary under the influence of a 15 kV potential applied across the length of the 60 cm capillary with a linear flow rate of $2.6 \times 10^{-3} \text{ m/s}$.

The broad features seen in Figure 13 are characteristic for dopamine, which has a relatively fast linear flow rate through an unmodified separation capillary. The relatively fast flow rate will influence the concentration in the volume surrounding the capillary opening to a larger extent in during these SECM measurements. Due to this fact,

subsequent measurements were performed using 2, 3-dihydroxybenzoic acid which exhibited a linear flow rate that was approximately half that of dopamine.

3.2 Imaging 2, 3-dihydroxybenzoic Acid Eluting from Separation Capillaries

Images similar to that of dopamine elution can be obtained using a solution of 2,3-dihydroxybenzoic acid continuously flowing through a 20 μm inner-diameter capillary (Figure 14). With the 2,3-dihydroxybenzoic acid, however, the current falls off much more rapidly from the peak value. Measurable current extends only approximately 250 μm in all directions from the current maximum with the 2,3-dihydroxybenzoic acid data. The current decreases 10% from the maximum value within ~ 25 μm , and by 25% within ~ 48 μm of the position where the current maximum is found.

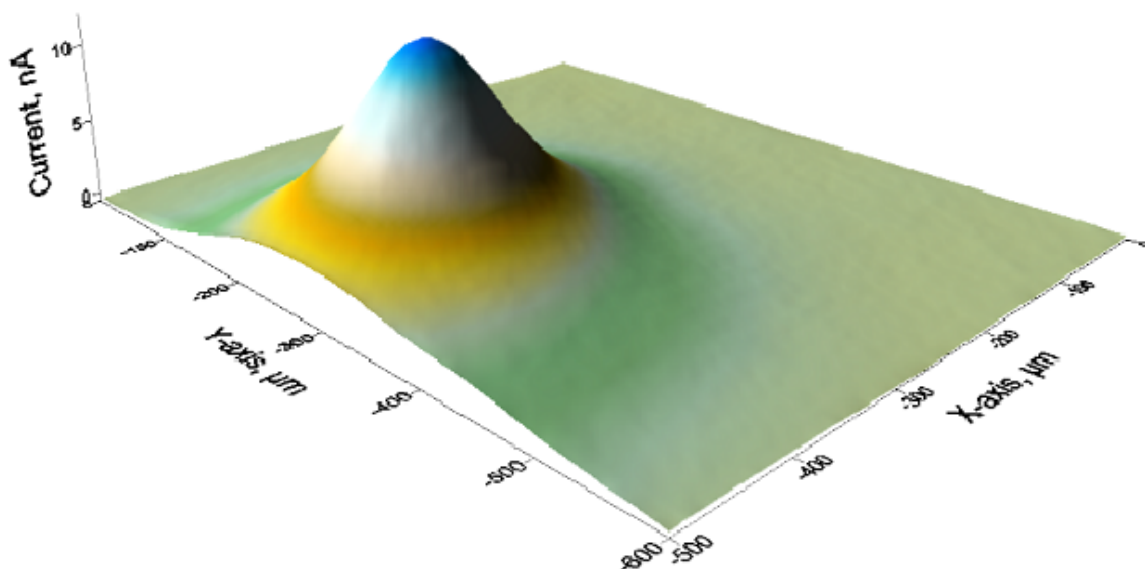


Figure 14. Image of 2,3-Dihydroxybenzoic acid as it emerges from the end of a 20 μm capillary. A 0.020 M 2,3-dihydroxybenzoic acid/phosphate buffer solution is continuously flowing through the capillary under the influence of a 15 kV potential applied across the length of the 60 cm capillary with a linear flow rate of 1.7×10^{-3} .

Examining the image in Figure 14, the peak is dramatically sharper than that obtained for dopamine. The difference in these two images can be attributed to the different rates at which these materials flow through the capillary. Dopamine, under the experimental conditions, has a linear flow rate of 2.6×10^{-3} m/s, while the 2,3-dihydroxybenzoic acid has a linear flow rate of 1.7×10^{-3} m/s. As the dopamine emerges from the capillary at a rate approximately 50% greater than that of 2,3-dihydroxybenzoic acid, it will influence the concentration in the volume surrounding the capillary opening to a larger extent in these measurements. For that reason, subsequent measurements using smaller inner diameter capillaries were conducted only with the 2,3-dihydroxybenzoic acid.

Using smaller capillaries in CE has a number of advantages including aiding in heat dissipation, using smaller volumes of solution, and decoupling the electric field of the UME from the applied separation voltage. Using a capillary with approximately the same inner diameter as the UME tip optimizes the signal-to-noise ratio as the noise is reduced without decreasing the effective concentration surrounding the UME. Smaller inner diameter capillaries have a steeper concentration gradient surrounding the capillary opening, thus, unless perfect alignment is achieved the S/N is dramatically reduced. Figure 15 shows the concentration profile of the 2,3-dihydroxybenzoic acid as it emerges from a 10 μm inner-diameter capillary. Due to the smaller capillary diameter, the concentration profile is much sharper than is found with a 20 μm inner-diameter capillary. With the 10 μm capillary, the current decreases by 10% within 20 μm of the maximum; by 25% within 30 μm of the maximum; and by 50% within 60 μm of the position where the maximum current is measured. The rapid fall-off in the current from

the peak value with the 10 μm inner-diameter capillary illustrates the importance of electrode placement when using capillaries with small inner diameters.

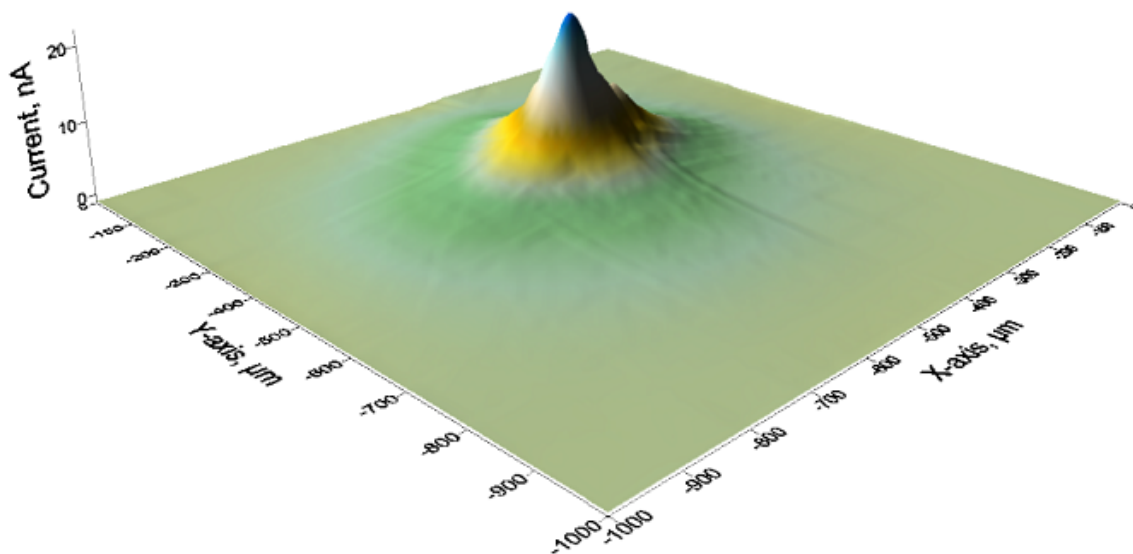


Figure 15. Image of 2,3-dihydroxybenzoic acid as it emerges from a 10 μm capillary. A 0.020 M 2,3-dihydroxybenzoic acid/phosphate buffer solution is continuously flowing through the capillary under the influence of a 15 kV potential applied across the length of the 60 cm capillary at a linear flow rate of 1.7×10^{-3} m/s.

In addition to the decrease of the detector current as the electrode is moved laterally away from the capillary opening, the peak current measured as zones of 2,3-dihydroxybenzoic acid emerge from the 10 μm capillary are found to decrease as the detector is moved further away, in the z-direction, from the capillary opening (Table 1). As one would expect, the detector current is largest when placed close to the capillary and decreases exponentially as the electrode is moved away from the capillary opening. We also found that the baseline noise (measured as either the standard deviation of the baseline current or the peak-to-peak variation of the baseline for 60 seconds prior to solute zones emerging from the capillary) decreased steadily as the electrode is moved from adjacent to the capillary opening to 30 μm away from the capillary opening (Table 1). Both the baseline standard deviation and the baseline peak-to-peak variation become

relatively constant when the electrode is further than 30 μm away from the capillary opening. This result is consistent with decoupling the detection from the current associated with the electrophoretic field with distance. Combining the peak current and the baseline noise as a function of distance from the capillary opening, it can be seen that the signal-to-noise is highest when the electrode is adjacent to the capillary opening, but is not appreciably larger than that found when the electrode is 10 μm or 20 μm above the capillary opening.

Table 1. Comparison of the peak current, baseline peak-peak noise, and baseline standard deviation as a function of electrode distance above the capillary opening obtained for a series of 5-second electrokinetic injections of 2 mM 2,3-dihydroxybenzoic acid.

Electrode Distance (μm)	Average Peak Current (nA)^a	Baseline Peak-Peak Noise^b	Baseline Standard Deviation (nA)^b
0	10.3 (± 1.9)	0.7	0.13
10	6.3 (± 0.6)	0.5	0.095
20	4.5 (± 0.6)	0.4	0.081
30	2.0 (± 0.2)	0.2	0.049
40	1.3 (± 0.2)	0.2	0.051

^aAverage of 5 electrokinetic injections, 5 seconds at 15 kV.

^bMeasured over 60 seconds prior to analyte peaks emerging from the capillary.

When aligning the electrode by these SECM measurements, the electroactive analyte is flowing continuously from the capillary. The concentration fall-off moving laterally away from the capillary opening will be even greater in actual CE separations where analyte emerges from the capillary as transient zones of material; consequently, electrode placement is even more critical for sensitive detection when using CE with electrochemical detection to analyze real-world samples. This is illustrated by acquiring a series of electrophoregrams in which varying amounts of 2,3-dihydroxybenzoic acid are introduced electrokinetically for 5 seconds. The resulting electrophoregrams can be used

to establish limits of detection and assess the extent to which automated SECM alignment outperforms manual alignment during actual CE separations.

3.3 Limits of Detection for Manual UME Alignment versus SECM UME Alignment

Automated SECM alignment allows for a more reproducible, accurate electrode placement than that manually under observation of a stereomicroscope. This is best illustrated by performing a series of injections in which varying concentrations of 2,3-dihydroxybenzoic acid are introduced electrokinetically for 5 seconds, conditions typical of analyses by capillary electrophoresis (Figure 16). One set of electrophoregrams is obtained after aligning the microelectrode manually, under the observation of a stereomicroscope; and the other data set is subsequently obtained after allowing the SECM to reposition the electrode as described above. All of these measurements were conducted with a 10 μm inner diameter capillary. The CE peaks for the 2,3-dihydroxybenzoic acid were, on average, approximately two times larger after the electrode placement was adjusted by the SECM (Figure 16).

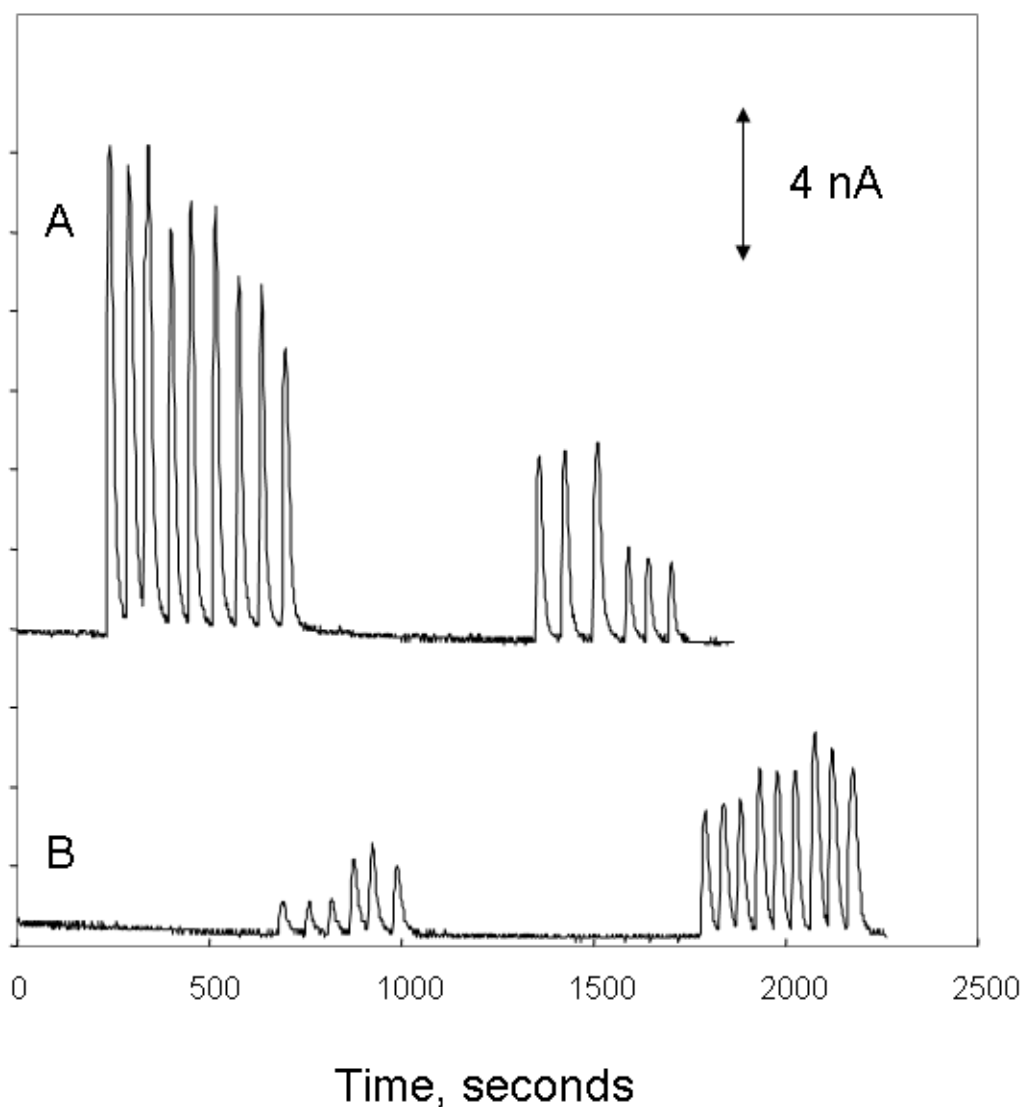


Figure 16. Comparison of multiple injections of varying amounts of 2,3-dihydroxybenzoic acid detected by square-wave electrochemical detection when the microelectrode is aligned manually (B) and then aligned by the SECM (A). For each alignment, a series of 3 injections of 5 different amounts of 2,3-dihydroxybenzoic acid (260 fmole, 180 fmole, 130 fmole, 79 fmole, and 26 fmole) are introduced to the capillary using 5 second electrokinetic injections.

The limit of detection (LOD) for 2,3-dihydroxybenzoic acid was determined for both the manually aligned microelectrodes and the SECM aligned microelectrodes when using a 10 μm inner diameter capillary. LOD values (to a 95% confidence) are determined by taking three times the standard deviation of the mean background signal

and dividing by the slope of the calibration curve (Figure 17) generated from the corresponding electropherogram in Figure 16. The result is the LOD in mM, which can then be converted to moles. Due to the imperfect geometry of the electrode tips, a cone shaped diffusion zone of volume $1/3\pi r^2 h$ is assumed, where r is the radius of the ID of the capillary (10 μm) and h is the height of any exposed section of carbon fiber (assumed to be 1 μm). When manually aligned, the limit of detection was 8.2 fmol of 2,3-dihydroxybenzoic acid. For the SECM aligned microelectrodes, the limit of detection was 3.8 fmol. These results are consistent with the SECM alignment, locating the position of maximum sensitivity much more accurately than manual alignment.

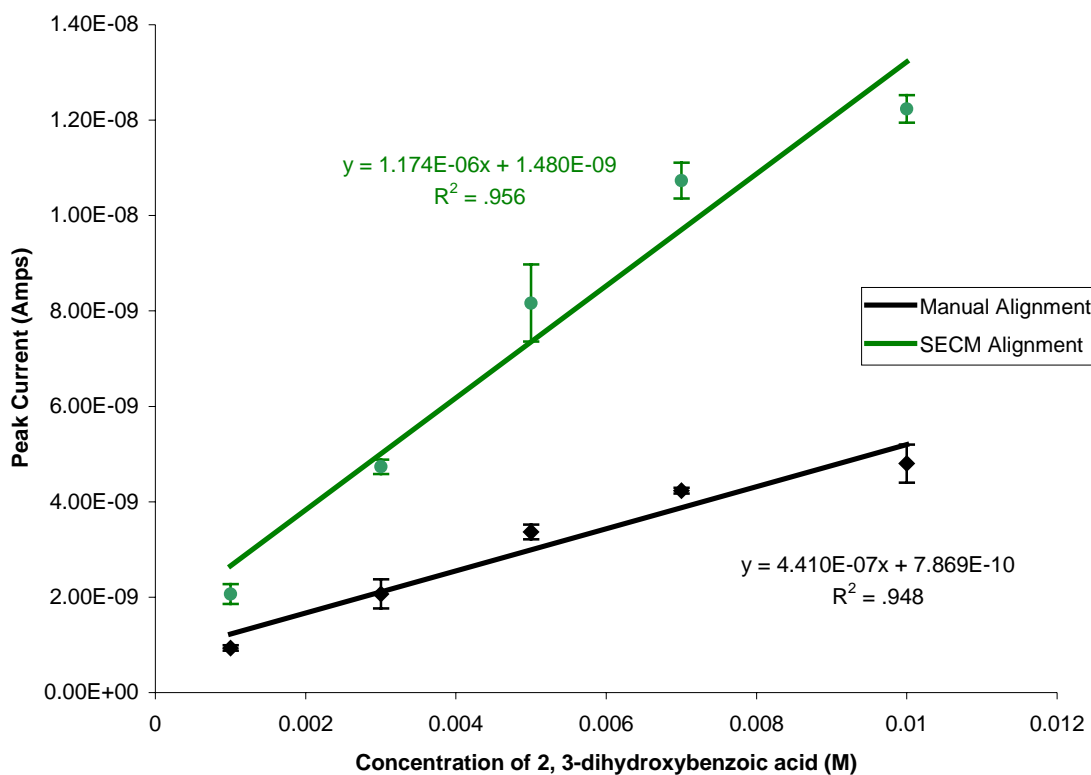


Figure 17. The calibration curves generated from electropherograms in Figure 15 establish the LOD for detection of 2, 3-dihydroxybenzoic acid for both a SECM aligned UME and a manually aligned UME.

3.4 Summary

These results illustrate that SECM placement of the electrode relative to the opening of the CE capillary results in consistently better detection sensitivity. The higher peak currents acquired when the SECM places the electrode is a function of the ability of the SECM to accurately locate the position where the analyte concentration is highest. The images of the electroactive material emerging from the 10 μm capillary show that misalignment of the electrode by an amount approximately equal to the diameter of the microelectrode can result in a 10-25% decrease in the detector signal. This is illustrated by the lower detection limits for 2,3-dihydroxybenzoic acid found when the microelectrode is aligned by the SECM compared (3.8 fmol) with that obtained with manual alignment (8.2 fmol). Furthermore, the best signal-to-noise with end capillary electrochemical detection is obtained when the detector electrode is placed just outside to the capillary opening; however, there is not an appreciable decrease in the signal to noise as the electrode is moved away from the capillary opening up to a distance of 20 μm .

It is reasonable to assume that SECM placement of the microelectrode would also result in better reproducibility in the detection. This, however, was not observed, as indicated by the relative standard deviation of the CE peaks obtained when the system is manually aligned (RSD = 7.0%) compared to the RSD values obtained after SECM alignment (RSD = 5.8%). The comparable RSD values were attributed to variability in the volume of material introduced during the manual electrokinetic injections. Electrokinetic injections were performed manually using a watch to measure the five-second injection. Computer controlled injections most likely would have lowered the RSD.

With the small absolute amounts of materials that emerge from the capillary during an electrophoresis experiment, the ability to place the electrode at the point of maximum sensitivity is critical to obtaining the best signal-to-noise in the analysis. This is especially true when using small inner-diameter capillaries where the size of the capillary opening is approximately the same as the size of the microelectrode used in the detection. Routine use of electrochemical detection for capillary electrophoresis in an analytical laboratory requires that accurate, reproducible alignment of the electrode with the capillary opening be easily obtained. The use of the SECM to position the electrode can achieve this goal automatically with minimal user intervention.

Chapter 4: Scanning Electrochemical Microscopy on Gold: Surface Imaging

4.1 Principles of Surface Imaging via SECM

Imaging of surfaces in SECM is performed in one of two different modes: tip generation/substrate collection mode or feedback mode^{25, 62}. The tip generation/substrate collection mode is characterized by monitoring both the tip current and the substrate current simultaneously. In the more commonly used feedback mode of SECM operation, the UME tip is rastered in close proximity to the substrate surface and a map of the electrochemical response of the tip as a function of position is produced. Feedback mode relies on an electrochemical mediator species to monitor both the surface topography and electrochemical reactivity of a substrate. As described earlier in *Chapter 1: SECM Description*, feedback can be either positive or negative depending on whether the substrate is conductive or insulating.

In positive feedback imaging, the mediator is electrolyzed at the UME tip and then oxidized/reduced to its original oxidation state via electron transfer at a conductive substrate surface. The closer the tip is to the substrate surface, the less the regenerated mediator is able to diffuse away into solution; thus, the effective concentration of the mediator in its original oxidation state is higher at small UME tip/substrate separation distances. The observed effect of feedback is an increase in current at a UME tip when it is held directly above a conductive substrate. In negative feedback imaging, the mediator is electrolyzed above an insulator and no electron transfer from the substrate is observed. The result is a lower concentration of mediator in its original oxidation state and a smaller observed current at the UME tip.

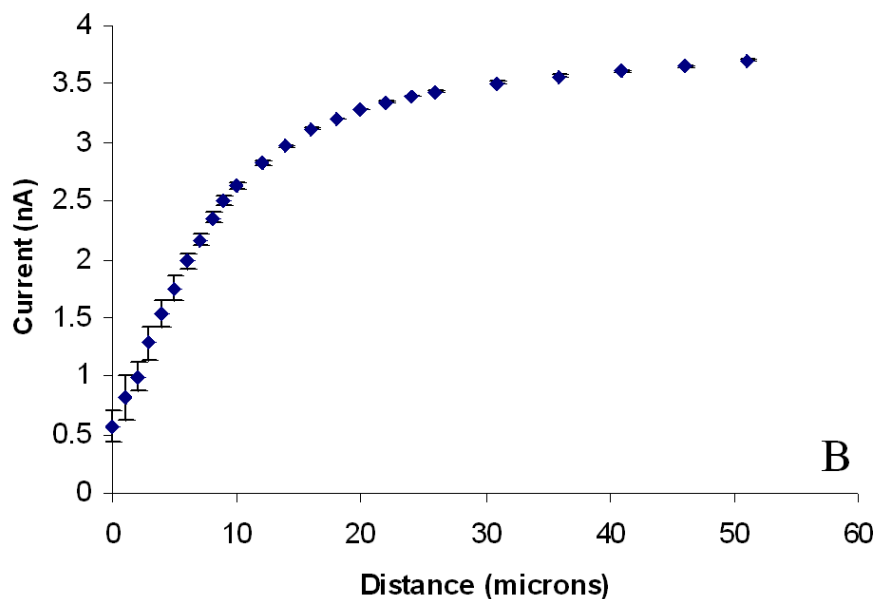
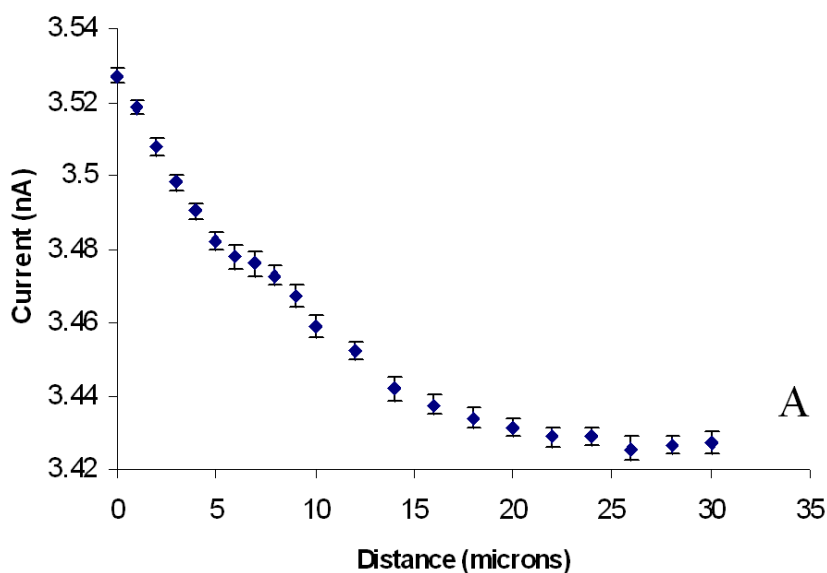


Figure 18. Approach curves generated by moving a 10 μm diameter Pt UME at 600 mV vs. Ag/AgCl close to a surface in a solution of 5 mM $\text{K}_4\text{Fe}(\text{CN})_6$ and 0.1 M KCl. When the tip approaches a conductor (A) feedback current is observed from the substrate; however, when the tip approaches an insulator (B) diffusion to the UME tip is hindered and the current decreases.

The effect of feedback can best be illustrated by examining a pair of approach curves (Figure 18) generated by moving a 10 μm diameter Pt UME approximately 10 μm

above a surface. Approach curves are generated by manually positioning the UME tip close enough to the substrate to observe a perturbation of the steady-state current, moving the UME a distance away, and then monitoring the current as the UME approaches its original position above the surface of a conductor (Figure 18A) and an insulator (Figure 18B). Above the conductive substrate the current is enhanced as the UME tip approaches the surface due to feedback; however, above an insulating substrate the current is greatly decreased as diffusion of $\text{Fe}(\text{CN})_6^{4-}$ to the UME tip is hindered by the surrounding insulator. These approach curves clearly demonstrate the ability of the SECM to effectively discriminate between a conductor and an insulator. Spatially resolving insulating/conductive domains can, therefore, be performed by rastering the UME probe at a constant 10 μm UME tip/substrate separation distance about a surface.

4.2 SECM Imaging of MDEA Surfaces

Imaging of chemically heterogenous substrates can be illustrated by examining SECM images of a multi-disk electrode arrays (Figure 19 and 20). Multi-disk electrode arrays (MDEAs) provide a complex surface which one can use to fine-tune the SECM to observe features with very small dimensions. For initial instrument testing, a 100 μm diameter disk MDEA provides a surface that can be easily characterized via SECM. By holding the UME tip 10 μm above the conductive disks, a current increase is observed; however, when the UME tip moves laterally above the transparent insulating portion of the MDEA, the current is decreased. The resulting image illustrates the disk position, size, and shape as well as the spacing between the disks. Disks of very small dimensions that are difficult to view with the naked eye are easily seen with the SECM.

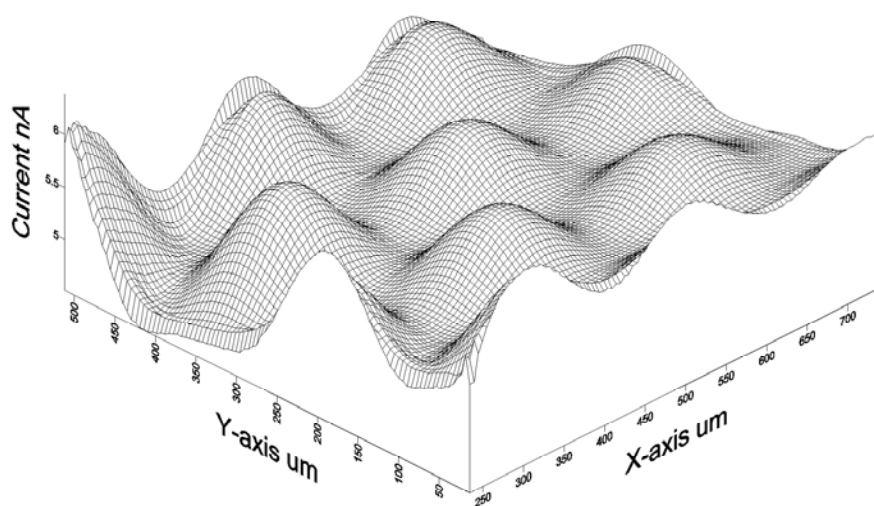


Figure 19. A wireframe SECM image of a 460 x 500 μm section of a MDEA shows peaks that illustrate the 100 μm diameter disks and the valleys that illustrate the insulating material that separates the disks. Experimental conditions: 10 μm Pt UME at 600 mV vs. Ag/AgCl, 5 mM $\text{K}_4\text{Fe}(\text{CN})_6$, and 0.1 M KCl.

Imaging 100 μm diameter MDEA disks provides a simple way to test an SECM instrument; however, imaging features closer to the size of the UME probe is much more desirable for most SECM applications. In order to ensure that smaller features could be observed with the SECM, a MDEA with 50 μm diameter disks was subsequently imaged (Figure 20).

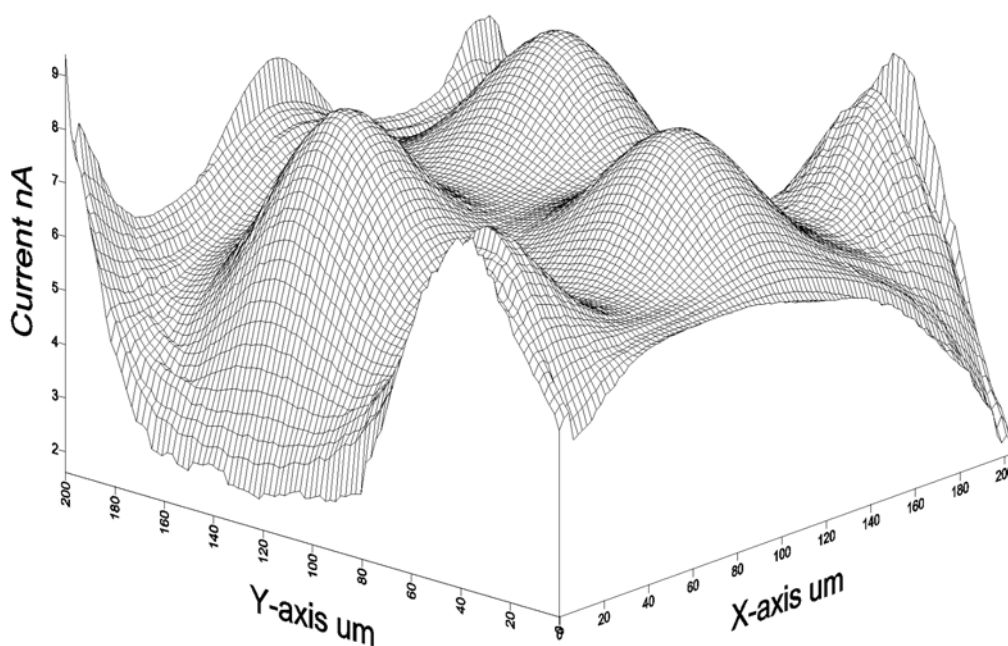


Figure 20. A wireframe SECM image of a 200 x 200 μm section of a multi-disk electrode array shows peaks that illustrate the 50 μm diameter disks and the valleys that illustrate the insulating material that separates the disks. The image was obtained using 5 mM $\text{K}_4\text{Fe}(\text{CN})_6$ and 0.1 M KCl as the mediator species and electrolyte species respectively in solution. The applied UME oxidation potential was 600 mV vs. Ag/AgCl.

When imaging features of this size, diffusion of the mediator species does not significantly blur the image resolution with features of this size. This is an important observation as it demonstrates that elements of similar size (50 μm) patterned into gold substrates can be unambiguously identified when they are as spaced as close as 50 μm .

After this initial testing of the SECM instrument on pre-patterned substrates, imaging of smaller sized features and SECM surface patterning/imaging of gold substrates can commence.

Chapter 5: Scanning Electrochemical Microscopy of Modified Gold Surfaces: Surface Patterning and Manipulation

5.1 Patterning Gold Substrates via Molecular Self-Assembly and Site Selective Desorption: An Introduction

Molecular self-assembly of n-alkanethiols onto gold substrates is a well established procedure⁶³⁻⁶⁵, and is known to result in the formation of a densely packed well-ordered interfacial structure of the n-alkanethiol along a gold surface. Self-assembly of n-alkanethiols onto Au (111) substrates result in coverages of approximately 7.8×10^{-8} moles/cm²^{38, 66, 67}. This corresponds to a $\sqrt{3} \times \sqrt{3}R30$ unit cell with approximately 4.9 Å spacing between the adjacent thiol molecules⁶⁸. The density of this hydrophobic layer prevents significant interaction between the gold substrate and the adjacent solution, effectively passivating the surface toward electrochemical reactions⁶⁹⁻⁷¹. Furthermore, adsorption of the longer chain n-alkanethiols lowers the surface energy of the substrate, thus, preventing adsorption of highly polar molecules along the surface⁷².

Once a gold surface is passivated with n-alkanethiol, the passivating layer must be removed in specific locations to produce a pattern of bare gold on the substrate to be used for subsequent surface modification. The technique most commonly used to remove n-alkanethiols from a gold surface is reductive desorption. Reductive desorption is a one electron process, by which, a n-alkanethiol can be removed from the surface of a gold substrate. For alkanethiols adsorbed onto gold, the Au-S can be broken at an accessible potential (usually -0.8 V to -1.2 V vs. Ag/AgCl)⁷³. When performed in a basic solution, the reduced alkanethiol will diffuse away from the surface into solution.

The potential at which a n-alkanethiol desorbs from a depends two principal factors: chain length, and local environment. A n-alkanethiol adsorbed to a gold surface

is stabilized principally by lateral van der Waals interactions with adjacent chains; therefore, longer chain lengths desorb at more negative potentials⁷⁴. As stabilization of the alkanethiol is due to van der Waals interactions among the chains, at defects or edges of an alkanethiol structure the thiol chains are much less stabilized and desorb at potentials less negative than necessary to desorb the bulk material⁷⁵⁻⁷⁷. This is an important factor to consider when selectively desorbing thiol domains from the gold substrate surface.

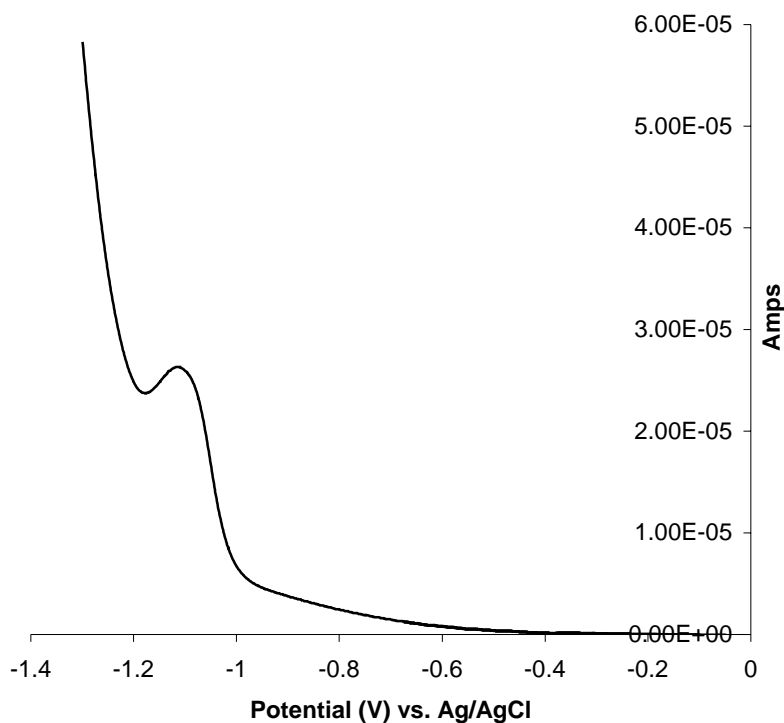


Figure 21. A typical bulk reductive desorption of a decanethiol monolayer from a 2 mm gold substrate in aqueous 0.5 M KOH.

Though completely removing n-alkanethiol from a gold substrate can be easily achieved using reductive desorption, a more discriminating technique called site selective desorption must be used to remove specific domains of alkanethiol; leaving the rest of the

passivating alkanethiol layer intact. Site specific desorption of n-alkanethiols has been demonstrated by Schuhmann^{36, 37}. This process takes advantage of the reductive desorption of alkanethiols at specific sites along the modified gold substrate using a Scanning Electrochemical Microscope (SECM)⁷⁴. Schuhmann demonstrated by using a UME as the auxiliary electrode and holding it close to a negatively biased gold substrate, the electric field is localized and the alkanethiol desorption is limited to those molecules in the region of the modified substrate opposite the UME. The resulting desorptions show dimensions and having approximately the same size as the exposed area of the UME^{36, 37}. Accurate movement and placement of a UME above an alkanethiol modified gold substrate, therefore, allows generation of an array of micrometer-sized features in which the n-alkanethiol has been removed by reduction of the Au-S bond. The exposed gold can then be subsequently modified for any number of chemical applications.

As site selective desorption is dependent on localizing the electric field, the size of the features desorbed depends primarily on the size and magnitude of the electric field. Using a smaller microelectrode will create a more localized electric field and thus a smaller area of desorption. Altering factors such as potential and ionic strength will also change the electric field and thus can be manipulated to change the size of the desorbed features. Applying a more negative potential will increase the size of the electric field and desorb more alkanethiol from the gold surface. Increasing the ionic strength of the solution will produce a similar effect and result in broader desorption features in the modified gold substrate. Here we report using site selective desorption to create features of different shapes potentially useful for enzyme deposition, and we illustrate how

changing ionic strength and applied potential affects the size of the features desorbed in the modified gold substrate.

5.2 Imaging Gold Substrates Patterned via Selective Desorption

Selective desorption of the n-alkanethiol from the modified gold substrate is performed by imaging the substrate using the feedback mode of the SECM. In these measurements, a 10 μm tip diameter Pt UME is moved in grid formation around the substrate at constant height in the presence of a redox couple that has reversible electrochemical behavior (e.g. $\text{Fe}(\text{CN})_6^{-4}/\text{Fe}(\text{CN})_6^{-3}$). The SECM probe is held at 600

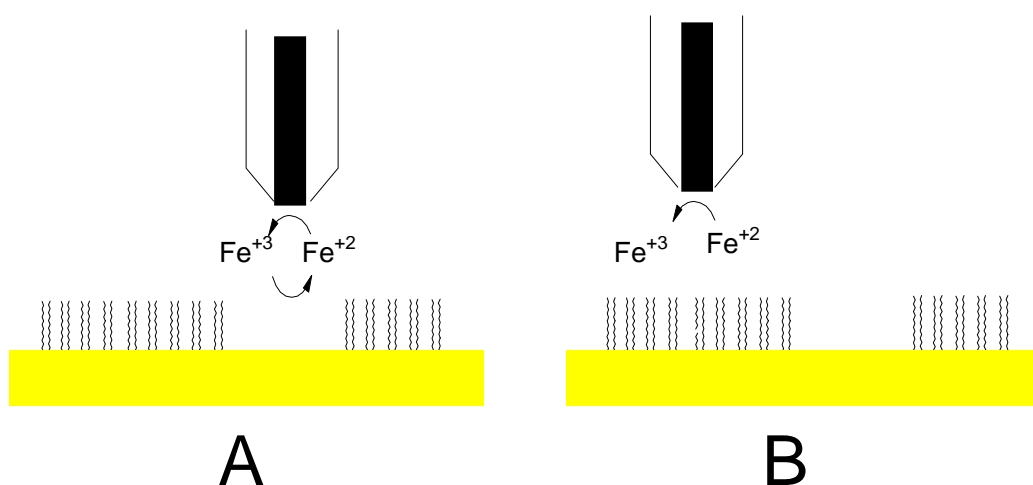


Figure 22. Schematic diagram of the SECM feedback imaging of the site specific desorption of the n-decanethiol monolayer.

mV, a potential that favors the oxidized form of the redox couple, and the gold substrate potential is held at 0 mV, a value that favors the reduced form of the redox couple. When the microelectrode is positioned over an exposed region of the Au substrate, the current measured at the microelectrode increases due to feedback from the gold surface (Figure 22A). Alternatively, when the microelectrode is positioned over a portion of the gold substrate in which the n-alkanethiol is intact, the current at the microelectrode is lowered

as the n-alkanethiol monolayer prevents reduction of the product of the oxidation at the UME (Figure 22B). As the microelectrode is moved along the x, y direction of the gold substrate at constant height, the magnitude of the oxidation current measured at the microelectrode SECM probe produces an image of the positions where site-selective desorption occurred. Based upon the size of the observed SECM features, the experimental conditions used for site selective desorption patterning is optimized to control the desorption feature size (e.g. applied potential, solution composition, microelectrode diameter, and size of the SECM scan).

5.3 Experimental Approach for Surface Patterning and Manipulation

Reagents

All aqueous solutions were prepared using 18M Ω deionized (DI) water (Barnstead Nanopure II). Decanethiol, octanethiol, absolute ethanol, KOH (99.99%), K₄Fe(CN)₆, NaCl, KCl, Na₂HPO₄, NaH₂PO₄, and NaOH were used as obtained from Sigma-Aldrich.

Scanning Electrochemical Microscopy

The SECM apparatus is as described in Chapter 2: *Experimental Details for Optimization of Electrode Alignment in Capillary Electrophoresis Using a Scanning Electrochemical Microscope*. The electrode potential for these measurements was controlled by a Cypress Systems EI-400 Bipotentiostat (Lawrence, KS). All applied potentials are referenced to an Ag-AgCl reference electrode. Both the grid size and step size of the scan, the desorption patterns, and all movement of the UME about the modified gold substrate is controlled via locally written software.

Modifying Gold electrodes

Gold electrodes 2 mm (CH Instruments) are modified by immersion in 1 mM n-alkanethiol in absolute ethanol and allowed to sit overnight. Electrodes can be used after only two hours of immersion; however, the electrodes were allowed to sit overnight to ensure dense packing and organization of the alkanethiol monolayer.

Electrochemical Measurements

The cell for the SECM measurements was produced locally in the Virginia Tech glass shop. Briefly, a 2 mm gold electrode is sealed inside a glass electrochemical cell by use of a tight o-ring in a Delrin base. The gold surface of the electrode sits vertically in a large (35 mL) reservoir that contains 20 mM KOH, 0.1 M KCl, and 5 mM $\text{K}_4\text{Fe}(\text{CN})_6$. During SECM feedback measurements, a 10 μm diameter disk Pt UME (CH Instruments) is used as the working electrode and is brought close ($\sim 10 \mu\text{m}$) to the gold surface of the 2 mm modified gold electrode. A Pt wire is sealed in the side of the glass reservoir as an auxiliary electrode, and the reference electrode is contained in a side neck of the glass reservoir. The Pt UME is biased to 600 mV vs. Ag/AgCl to ensure it is in the steady state region of the cyclic voltammetry curve (Figure 5), and the 2 mm gold electrode is held at a potential of 0 V. The electrode potential for these measurements was controlled by a Cypress Systems EI-400 Bipotentiostat (Lawrence, KS).

Site selective desorptions were performed in the same solution and same conditions; however, the Pt UME tip was used as the auxiliary electrode and the gold surface was used as the working electrode. Patterning was performed by moving the electrode above the modified gold surface using locally written software.

5.4 Site-Selective Desorptions Via SECM: Pattern Generation

Initial site selective desorptions were performed using the same solution used for imaging of the MDEA surfaces; however, 20 mM KOH was added to the solution to ensure that desorbed thiol would not reabsorb to the gold surface. The preliminary goal of these initial desorptions was to demonstrate control of the UME position above the substrate and establish a typical desorption feature size under these conditions. The first desorbed pattern generated in a decanethiol modified substrate was pair of 50 x 50 μm holes separated by 50 μm diagonally (Figure 23).

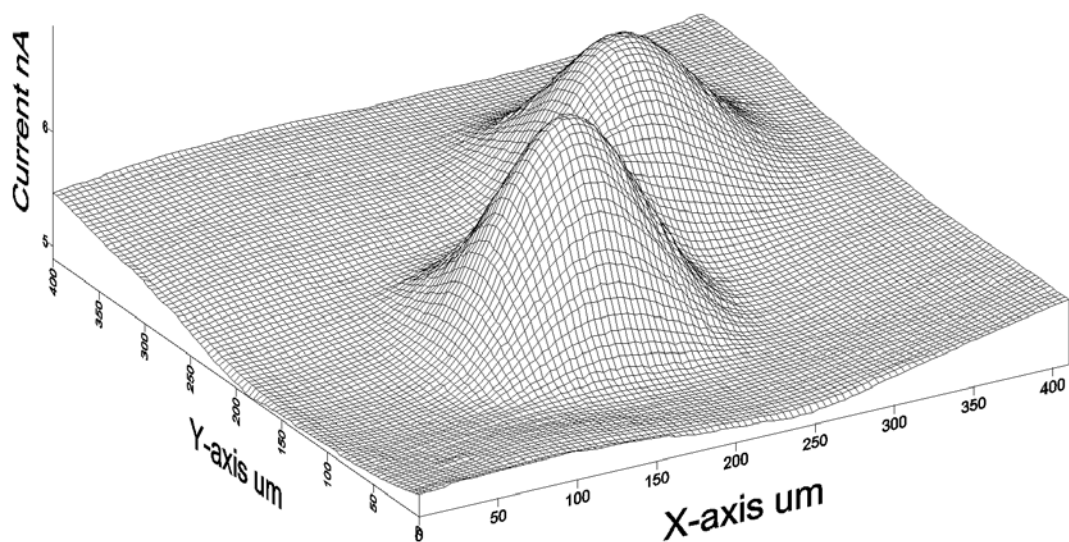


Figure 23. SECM image of two 50 x 50 μm holes desorbed at -1.0 V vs. Ag/AgCl in a decanethiol modified gold substrate separated by 50 μm diagonally. The resulting image illustrates the desorbed holes are roughly twice the dimensions over which the UME tip is rastered.

Upon imaging via feedback SECM, the resulting desorptions demonstrated feature sizes approximately four times larger in area than that over which the UME is

rastered. The size of the feature imaged via feedback SECM is expectedly larger than the actual desorptions, as the imaging relies on an electroactive species diffusing between the UME tip and the substrate surface. Following desorption of holes in a substrate, creating an island of alkanethiol in a gold substrate became the next desirable pattern to produce. Our lab has previously modified gold electrodes with functionalized alkanethiol chains and electrostatically bound enzymes to these electrodes. Creating specific domains of alkanethiol on a surface therefore allows for deposition of enzymes in specific domains along the substrate (conditions necessary for the generation of a biosensor array). As a proof of concept for this project, thiol islands were created via SECM site selective desorption (Figure 24).

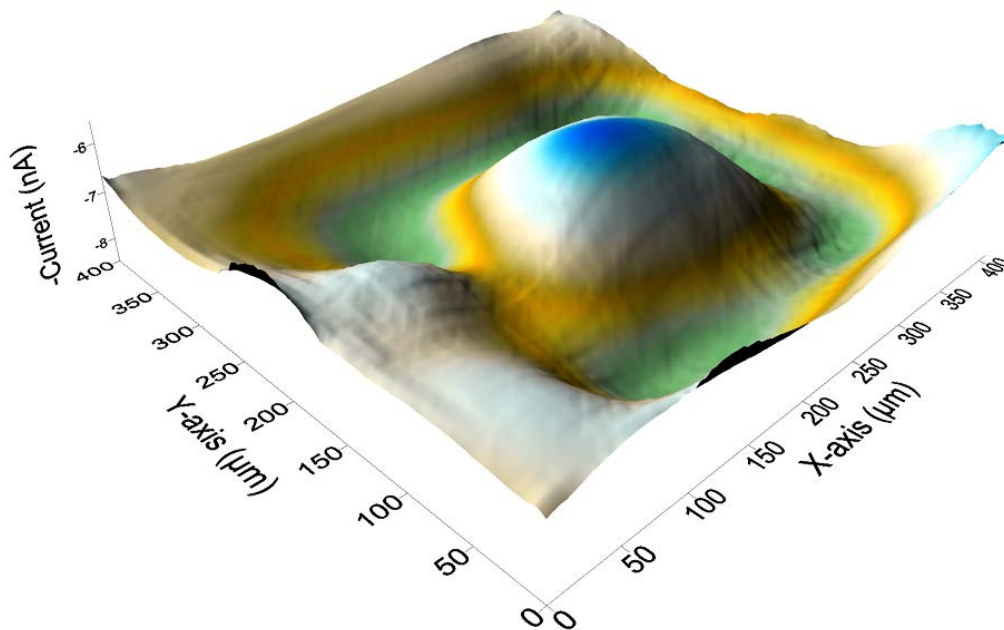


Figure 24. SECM feedback image of a 150 x 150 μm island of decanethiol desorbed from a decanethiol modified gold substrate. The UME tip has been rastered about a 200 μm square resulting in a decanethiol island surrounded by bare gold.

Figure 24 depicts a 150 x 150 μm alkanethiol island desorbed by rastering the UME in a 200 μm square about a modified gold substrate. The feedback image has been

inverted so that the island appears as a mountain (rather than a depression) in the middle of the figure. The feedback image clearly shows the thiol island surrounded by bare gold, which is in turn surrounded by the decanethiol from the bulk surface passivation.

Furthermore, the feedback image demonstrates the ability of the SECM to pattern small alkanethiol domains in a substrate by removal of surrounding mercaptan. Generation of a alkanethiol island also illustrates the capacity of the SECM to create the alkanethiol spots in a substrate as a base for subsequent enzyme deposition and biosensor assembly.

In order to further demonstrate control of the UME position and desorption, a “VT”, the college logo of Virginia Tech, was patterned in a decanethiol modified gold substrate (Figure 25). After demonstrating control of the UME tip and gross features desorbed in the modified gold substrate, research efforts shifted to more precisely controlling the size of the desorbed features in the substrate. To this end, both applied potential and ionic strength were studied as adjustable parameters that can be used to control desorption feature size.

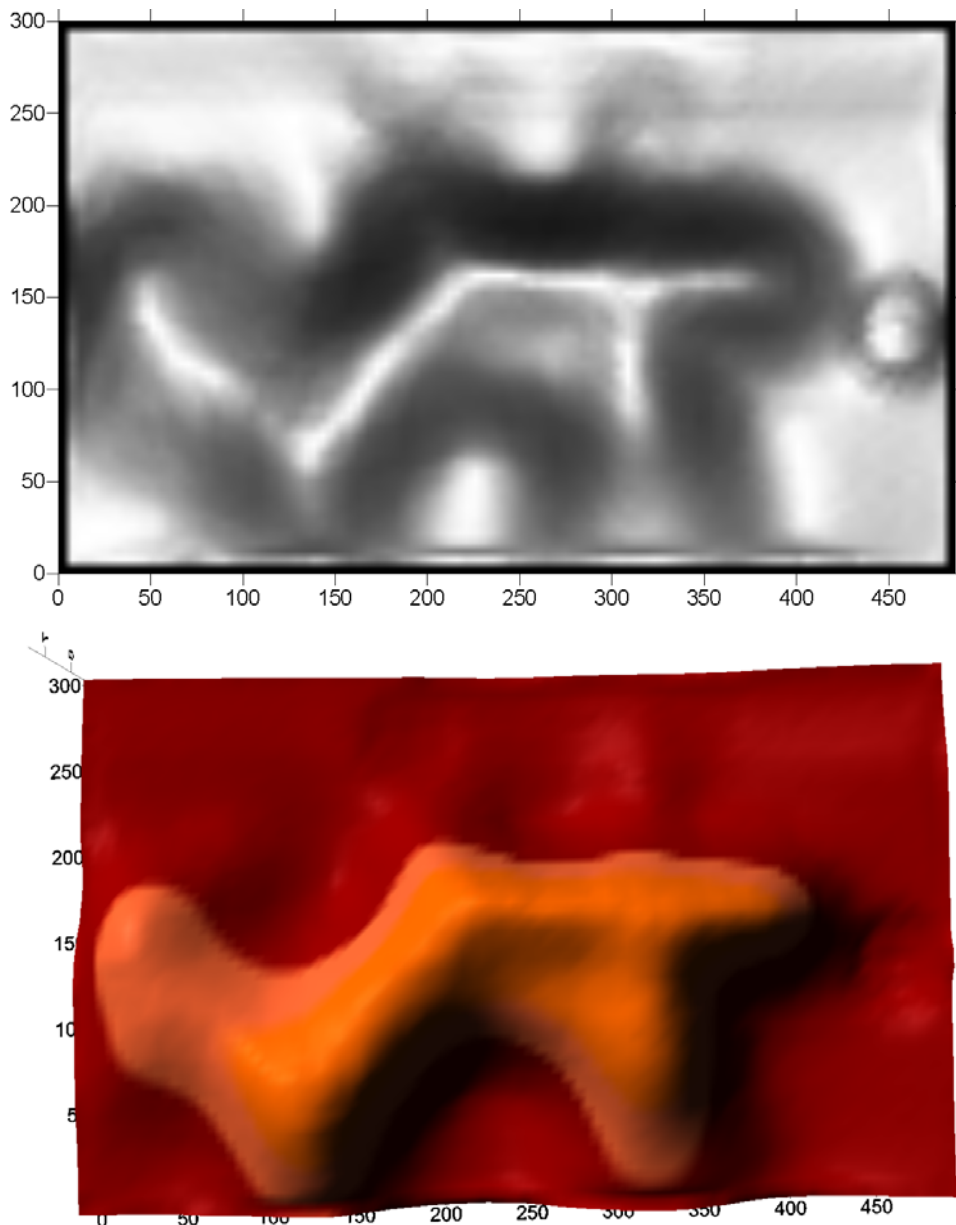


Figure 25. SECM feedback images of a “VT” desorbed at -1.0 V vs. Ag/AgCl from a decanethiol modified gold substrate. A shaded relief map (top) shows one representation of the “VT”, while a more familiar false color image (bottom) shows the “VT” desorption from another perspective. All distances on the X and Y axes are in microns and the desorbed “VT” is approximately $200\ \mu\text{m}$ tall and $400\ \mu\text{m}$ long.

Chapter 6: Controlling Desorbed Feature Size on a Modified Gold Substrate

6.1 Feature Size as a Function of Potential

When patterning a thiolated gold surface using a SECM, the modified gold substrate is held at a bias potential relative to the Ag/AgCl reference and the UME tip is used as the auxiliary electrode. The electric field is therefore isolated in the region below the UME tip, and redox chemistry occurring in this volume of space is controlled by the distribution of the electric field between the UME and the substrate²⁵. The electric field (E) between two parallel plates (eq 5) is dictated by the distance (d) between the plates and the potential difference (V) applied to the plates; therefore, increasing the applied potential increases the magnitude of the electric field and the area over which the electric field can influence reaction chemistry⁴.

$$E = V/d \quad (5)$$

By changing the electric field strength, the area over which electrochemical desorptions of thiol from a gold substrate can be altered. This is demonstrated by

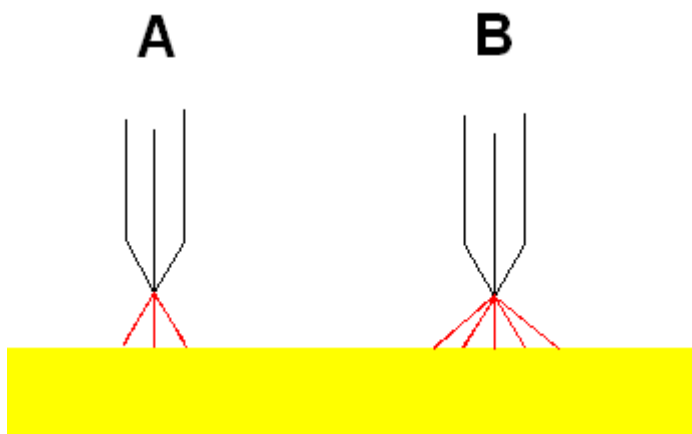


Figure 26. When a small potential is applied the electric field is localized to a small region between the UME tip and the substrate (A). If a larger potential is applied the area over which the electric field can affect the substrate is increased (B).

desorbing (using different potentials) three 300 μm lines from a gold substrate at a constant UME/substrate distance (Figure 27). The SECM image of the resulting desorptions shows three distinct lines in the substrate. The lines are the desorbed regions of bare gold in the passivated substrate that allow feedback current to occur. The applied potential used for desorption becomes more negative from the bottom to the top line. As the potential is made more negative the desorbed line becomes larger in area and produces a greater amount of feedback during SECM imaging (Table 2). The increase in line width can be attributed to the increase in the magnitude of the electric field between the UME tip and the gold substrate. The increase in the feedback current associated with more negative desorption potentials is attributed to the larger area of gold available to provide feedback to the UME tip. Furthermore, applying a more negative potential to the surface provides a more efficient desorption, ensuring no small domains of thiol remain bound to the gold—thus hindering feedback during an SECM imaging scan.

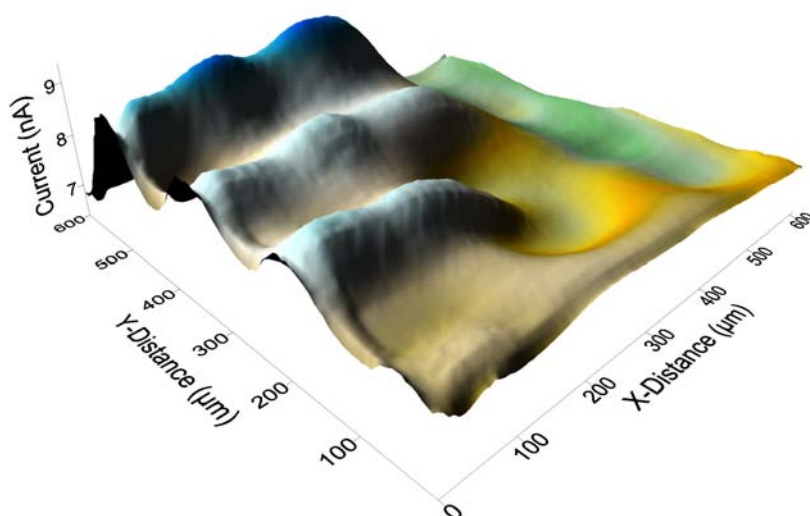


Figure 27. False color image of three lines desorbed from a decanethiol modified gold substrate. The desorption are at -1.1 , -1 , and -0.9 respectively from the top to the bottom vs. Ag/AgCl . Imaging conditions: 0.1 M KCl , 5 mM $\text{K}_4\text{Fe}(\text{CN})_6$, 20 mM KOH .

Table 2. Size of features and feedback current data for lines desorbed from a decanethiol modified gold substrate at different potentials.

Applied Desorption Potential (V vs. Ag/AgCl)	Peak width (μm) at 8.2 nA	Peak height (nA) at X- distance of 200 μm
-0.9	68	8.4
-1.0	74	8.6
-1.1	94	9.0

Subsequent desorptions under the same conditions exhibited similar features; however, at -0.9 V the desorptions were often inefficient. While inefficient, patchy desorptions were observed at -0.9 V, potentials more positive of this were insufficient to desorb any decanethiol from the surface of the gold. The patchy lines for the desorption of decanethiol at -0.9 V gives support to the observation that desorptions are initiated at defect sites in the monolayer that require less charge to remove than the bulk material⁷⁵⁻⁷⁷. In multiple trials, lines desorbed at -0.9 V and subsequently imaged resembled a linear array of desorbed holes rather than a continuous desorption line (Figure 28). The application of SECM to study defect sites in monolayers is an attractive area of research and will be a subject of future study in relation to the work presented here.

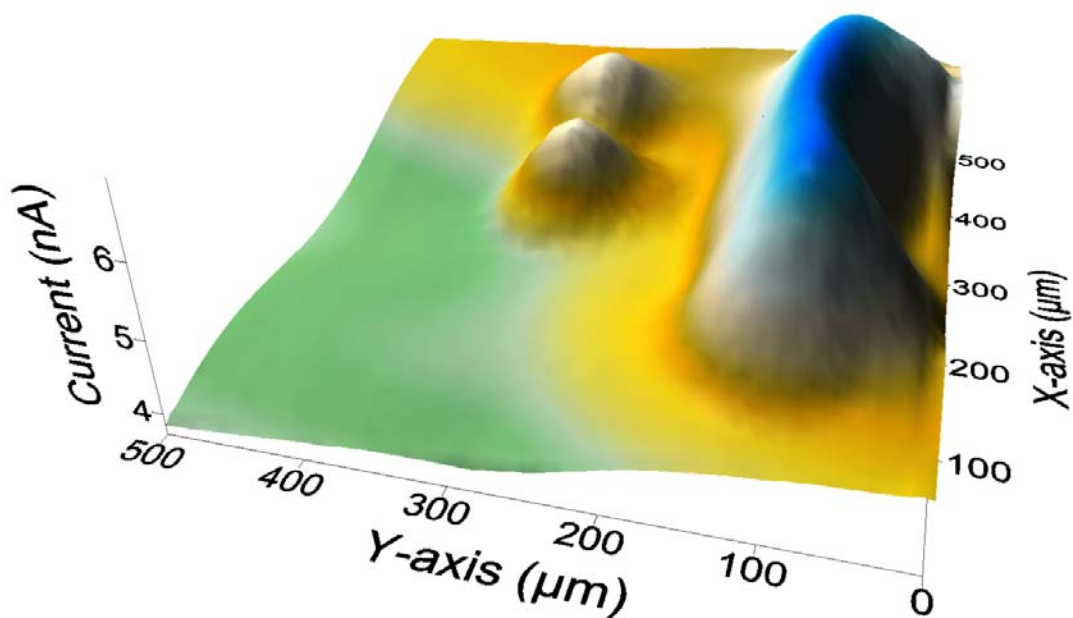


Figure 28. Two lines desorbed in a decanethiol modified gold substrate. The line desorbed at -1.0 V (pictured right) demonstrates a continuous desorption of thiol. The line desorbed at -0.9 V (pictured left) appears as two small desorbed holes in the monolayer. The patchy desorption at -0.9 V is consistent with the theory that desorptions are initiated at defect sites in the monolayer.

6.2 Feature Size as a Function of Ionic Strength

While changing the magnitude of the electric field can be accomplished by using a more negative potential for desorption, ultimately this method is limited by the useable potential range established by the solvent used for desorption electrochemistry. By changing the ionic strength of a solution, the electric field along the gold substrate is controlled by altering the resistivity of the solvent used for desorption. In a more resistive solution, the electric field between the UME and the gold substrate is localized by increasing the resistance between the two conductors, effectively decreasing the lateral distance over which the potential difference is perceived by the gold surface. The result of this localization is a smaller desorption area and another method with which desorption feature size can be controlled.

The localization of desorption phenomena by controlling ionic strength is best illustrated by desorbing three lines (using different ionic strength solutions) in a decanethiol modified substrate and imaging by feedback SECM (Figure 29). The resulting image depicts three desorbed lines of varying feature size. The line desorbed at the lowest ionic strength (top) exhibits the smallest area of desorption and the lowest amount of feedback current due to the localization of the electric field during desorption. As the ionic strength increases, both the area of the desorption features and the observed feedback current increase for same reasons described in the *Feature Size as a Function of Potential* section of this manuscript.

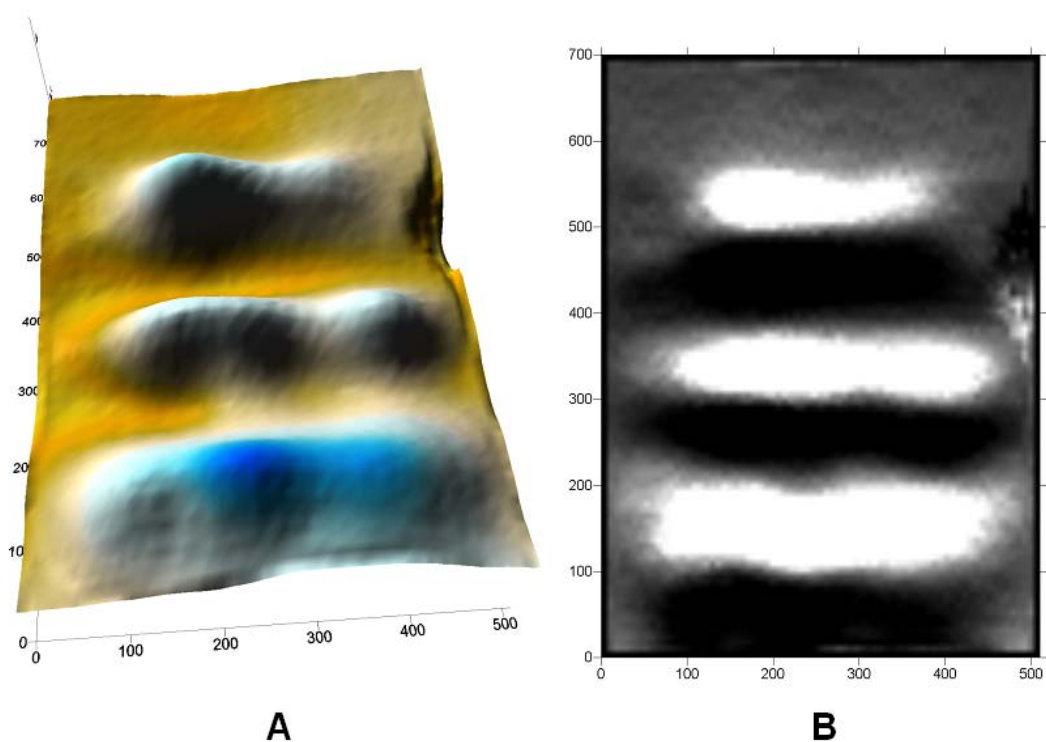


Figure 29. Three lines desorbed at ionic strengths of 0.05, 0.12, and 0.17 respectively from top to bottom using the same UME/substrate distance. A false color image of the desorptions (A) shows a map of the current as a function of distance while the shaded relief map (B) better illustrates the size of the desorbed holes in the decanethiol modified gold surface. All distances labeled on the axes are in microns (desorption potential -1.0 V).

A cross section of this SECM feedback image, Figure 30, better illustrates the effect of desorbing decanethiol at varying ionic strengths. Here, it is easier to view the width and current response of the desorptions created in the different ionic strength solutions. The cross section illustrates that using higher ionic strength solutions results in desorption lines that generate a greater feedback response, a result consistent with applying a larger electric field to the gold surface. The exact width of the desorptions is more difficult to analyze with SECM due to the fact that imaging is performed using a diffusing electrochemically active species. The diffusion to and from the substrate

surface distorts the resulting SECM image and exact width measurements of a desorption line are difficult to obtain. Examining the width of the desorption at a low SECM feedback currents (7.7 nA), it can be observed qualitatively that the line desorbed at the ionic strength of 0.17 exhibits the largest width of desorption (~200 μm), the line desorbed at an ionic strength of 0.12 has the next largest width of desorption (113 μm), and the line desorbed at an ionic strength of 0.07 has the smallest width of desorption (99 μm). Upon alteration of the existing setup to include the modifications of gold slides, the exact width of each line can be more accurately measured via AFM.

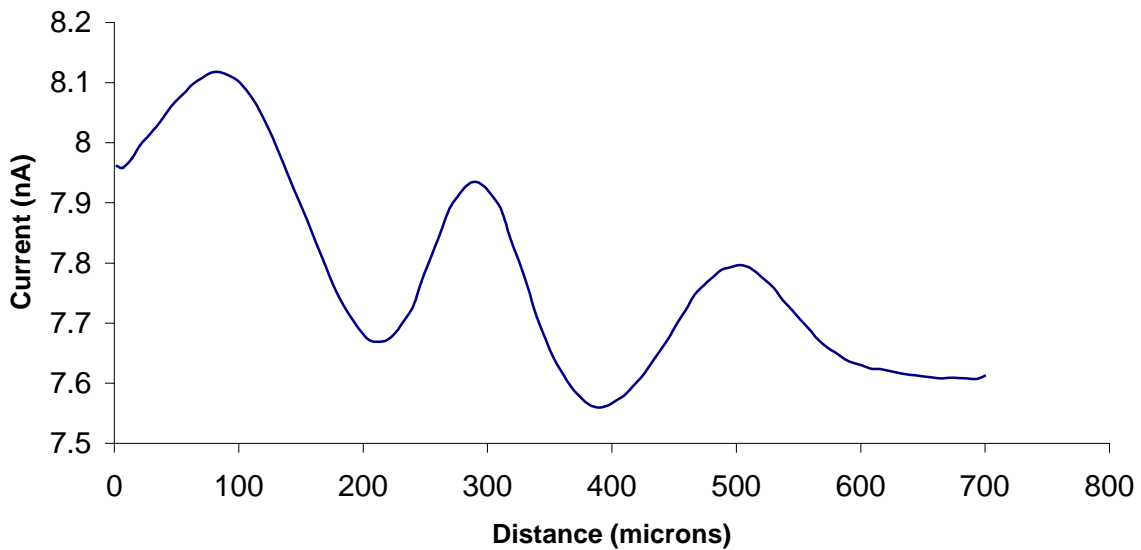


Figure 30. Cross section of three lines desorbed at ionic strengths of 0.07, 0.12, 0.17 from right to left. The increasing ionic strength increases effective electric field at the gold substrate. A larger applied electric field results in desorption lines of larger width and greater feedback response during SECM imaging.

6.3 Summary

These results illustrate the capacity of the SECM to image chemically heterogeneous substrates and pattern alkanethiol modified gold surfaces. A wide array of patterns potentially useful for enzyme deposition or local adhesion promotion can be inscribed into a modified gold substrate by SECM site selective desorption. Control over the size of the desorption features is achieved by controlling either the potential or the ionic strength at which the desorptions are performed. By applying a more negative desorption potential, the applied electric field is increased along with the area over which the desorption occurs. Increasing the ionic strength of the solution increases the area over which the applied potential is distributed, effectively enlarging the electric field and the area over which the passivating alkanethiol monolayer is desorbed.

While obtaining quantitative differences between the peak heights is not achievable due to the noise (0.2 nA) associated with the measured current; qualitatively, the trend of more complete desorption upon applying a more negative potential or operating in a higher ionic strength solution is certainly upheld. Examining the peak widths at low feedback currents, the width of the desorbed feature is undoubtedly dependent on the ionic strength of the solution and the applied desorption potential. Though exact measurements of desorption width are difficult to perform with SECM, due to the dependence of imaging on a diffusing electroactive species, using larger ionic strengths/more negative applied potentials increases the feature width significantly.

By closely controlling the ionic strength and the potential used for site selective desorption, the size of features desorbed in a modified gold substrate can be better controlled. As any lithographic technique is dependent on the resolution with which

features can be patterned into a substrate, manipulation of the feature shape and size in site selective desorption is absolutely critical for this method to become a more widely used surface patterning method. Precise control of ionic strength/desorption potential allows smaller features to be patterned in a substrate, and provides two parameters for tuning feature size using this lithographic technique.

Chapter 7: Summary and Future Work

7.1 Project Summary

This manuscript provides a detailed description of the SECM operation, SECM construction, and SECM application to a myriad of systems. SECM was initially applied to CZE to image the concentration gradient around the open end of a separation capillary while electroactive material continuously emerges. Software was subsequently written to place the UME probe at the position of maximum current (directly opposite the capillary opening) reliably and reproducibly. Studies of the effect of UME position on signal-to-noise were performed and it was shown the signal-to-noise does not dramatically decrease until the electrode is more than 30 μm above a 10 μm inner-diameter capillary. Limits of detection for 2,3-dihydroxybenzoic acid were found to be 8.2 fmol when the UME was aligned manually, and 3.8 fmol when the SECM is used to automatically align the microelectrode.

SECM was then used to image a MDEA to demonstrate the capacity of the SECM to image very small domains of conductor on an insulating substrate. The resulting images demonstrated the ability of the SECM to unambiguously identify two 50 μm diameter conductive domains separated by a mere 50 μm . Upon proving the ability of the SECM to resolve such small features, surface patterning of n-alkanethiol modified substrates using site selective desorption could commence. Various patterns were created on these modified gold substrates in order to demonstrate control of feature shape, and to provide a proof of concept for construction of biosensor array.

Finally, the effect of applied potential and ionic strength on the size of the desorbed features was analyzed. It was shown that by increasing the ionic strength of the

solution or by making the applied potential more negative the magnitude of the electric field at the modified gold substrate was increased and it was shown qualitatively that the desorbed features became broader in size. By controlling the ionic strength and the potential used for site selective desorption, the dimension of features desorbed in a modified gold substrate can be better controlled. As any lithographic technique relies on the resolution with which features can be patterned into a substrate, manipulation of the feature shape and size in site selective desorption is absolutely critical for this method to become a more widely used surface patterning method.

7.2 Future Work

The opportunities for building on the work described in this manuscript are innumerable; however, our research group plans to pursue three main research venues afforded by the versatility of this instrumentation. The three projects our group is most interested in are: 1) Constructing a Michelson interferometer to adjust the substrate tilt and measure fine movements of the inchworm actuator, 2) studying defects in self assembled monolayers by examining the existence of patchy desorptions using n-alkanethiols of varying chain lengths, and 3) constructing a biosensor array by deposition of enzymes onto thiol islands patterned on a gold surface.

By affixing a Michelson interferometer to our SECM setup we can control the substrate tilt (thereby avoiding tip crashes) by observation of an interference pattern. If the substrate is tilted relative to the z-axis of the SECM, an interference pattern will not appear because the laser light will not be reflected back to the interferometer.

Furthermore, fine movements of the z-actuator can be monitored by mounting a photodiode detector where the interference pattern is observed. When the stage with the

UME and the laser is moved a length equal to half the wavelength of the incident light the observed interference pattern will shift from constructive to destructive (or visa versa) thus enabling quantitative measurements of movements equal to half the wavelength of the laser light.

Examination of the patchy features that occur when performing site selective desorption using a potential insufficient to remove the bulk n-alkanethiol from a gold surface will continue. The studies will examine a range of chain lengths of n-alkanethiol with the working hypothesis that longer chain lengths will result in more patchy desorptions. If shorter chain length alkanethiols exhibit more defects in their structure, the desorptions will appear more continuous as the multiple defect sites will allow thiol to be removed from the surface more efficiently. Longer chain alkanethiols will exhibit more patchy desorptions as they have fewer defects sites and are more stabilized by van der Waals interactions. The results of these studies will be used to qualitatively illustrate the effect of alkanethiol chain length on number of defect sites in a monolayer. In addition to studies of how altering chain length can alter the number of defects in a monolayer, studies of how packing time affects defects in SAMs can also be performed by immersing a gold slide in a solution for a given amount of time, performing site selective desorption, and examining the desorption lines created in the substrate.

Finally, by using site selective desorption to pattern a number of functionalized thiol islands on a substrate, a biosensor array consisting of enzyme spots will be assembled on a gold substrate. Upon introduction of the proper substrate, hydrogen peroxide will be produced by the enzyme and will be monitored amperometrically via SECM. The initial construction will use glucose oxidase as a proof of concept; however,

once the technique is refined, an array of enzymes may be patterned onto surfaces to produce a biosensor capable of measuring multiple biologically important molecules.

References

1. Laidler, K. J. *The World of Physical Chemistry*; Oxford University Press: Oxford, 1993.
2. Birdi, K. S. *Scanning Probe Microscopies*; CRC Press: Boca Raton, FL, 2003.
3. Oatley, C. W. *Journal of Applied Physics* **1982**, *53*, R1-R13
4. Young, H. D.; Freedman, R. A. *University Physics*, 10th ed.; Addison Wesley: New York, 2000.
5. Young, R. D.; Ward, J.; Scire, F. *Rev. Sci. Instrum.* **1972**, *43*, 999
6. Binning, G.; Rohrer, H.; Gerber, C.; Weibel, E. *Physical Review Letters* **1982**, *49*, 57-61
7. Binning, G.; Quate, C. F.; Gerber, C. *Physical Review Letters* **1986**, *56*, 930-933
8. Bard, A. J.; Faulkner, L. R. *Electrochemical Methods: Fundamentals and Applications*, 2nd ed.; John Wiley and Sons: New York, 2001.
9. Park, S.; Barrett, R. C. *Scanning Tunneling Microscopy*; Academic Press: New York, 1993.
10. Fuchs, H. *Physica Scripta* **1988**, *38*
11. Yau, S. L.; Vitus, C. M.; Schardt, J. *Journal of the American Chemical Society* **1990**, *112*, 3677
12. Bard, A. J.; Kim, T.; McCarley, R. L. *Journal of Physical Chemistry* **1992**, *96*, 7416
13. Binning, G.; Rohrer, H., *Europhys. Conf. Abstr.*, 1982; 210.
14. Teague, E. C.; Scire, F. E.; Backer, S. M.; Jensen, S. W. *Wear* **1982**, *83*, 1-12

15. Atkins, P.; De Paula, J. In *Physical Chemistry*, 7th ed.; W. H. Freeman and Co.: New York, 2002, pp 686-712.
16. Drake, B.; Prater, C. B.; Weiserhorn, A. L.; Gould, S. A. C.; Albrecht, T. R.; Quate, C. F.; Cannell, D. S.; Hansma, H. G.; Hansma, P. K. *Science (Washington D. C.)* **1989**, *243*, 1586-1589
17. Hamers, R. J. *Journal of Physical Chemistry* **1996**, *100*, 13103-13120
18. Giessibl, F. J. *Science (Washington D. C.)* **1995**, *267*, 68-71
19. Alexander, S.; Hellemans, L.; Marti, O. S., J.; Elings, V.; Hansma, P. K. *Journal of Applied Physics* **1988**, *65*, 164-167
20. Skoog, D. A.; Holler, F. J.; Nieman, T. A. *Principles of Instrumental Analysis*, 5th ed.; Thomson Learning, Inc.: New York, 1998.
21. Ogoshi, T. F., T.; Bertolucci, M.; Galli, G.; Chiellini, E.; Chujo, Y.; Wynne, K. J. *Journal of the American Chemical Society* **2004**, *126*, 12284-12285
22. Frisbie, C. D.; Rozsnyai, L. F.; Noy, A.; Wrighton, M. S.; Lieber, C. M. *Science (Washington D. C.)* **1994**, *265*, 2071-2074
23. Forster, R. J. *Chemical Society Reviews* **1994**, *23*, 289-297
24. Fleischmann, M.; Pons, S.; Rolison, D. R.; Schmidt, P. P. *Ultramicroelectrodes*; Datatech Systems Inc.: Morganton, NC, 1987.
25. Bard, A. J.; Mirkin, M. V. *Scanning Electrochemical Microscopy*; Marcel Dekker, Inc.: New York, NY, 2001.
26. Bard, A. J.; Fu-Ren, F. F.; Pierce, D. T.; Unwin, P. R.; Wipf, D. O.; Zhou, F. *Science (Washington D. C.)* **1991**, *254*, 68-74
27. Mirkin, M. V.; Horrocks, B. R. *Analytica Chimica Acta* **2000**, *406*, 119-146

28. Wei, C.; Bard, A. J.; Mirkin, M. V. *J. Phys. Chem.* **1995**, *99*, 16033-16042
29. Wipf, D. O.; Bard, A. J. *Anal. Chem.* **1992**, *64*, 1362-1367
30. Lee, C. K., J.; Bard, A. J. *Proc. Natl. Acad. Sci.* **1990**, *87*, 1740-1783
31. Tsionsky, M.; Cardon, Z. G.; Bard, A. J.; Jacskon, R. B. *Plant Physiology* **1997**, *113*, 895-901
32. Pierce, D. T.; Unwin, P. R.; Bard, A. J. *Anal. Chem.* **1992**, *64*, 1795-1804
33. Pierce, D. T.; Bard, A. J. *Anal. Chem.* **1993**, *65*, 3598-3604
34. Hitoshi, S.; Tomokazu, M.; Uchida, I. *Anal. Chem.* **1996**, *68*, 1276-1278
35. Iva Turyan, T. M., Daniel Mandler *Anal. Chem.* **2000**, *72*, 3431 - 3435
36. Wittstock, G.; Hesse, R.; Schuhmann, W. *Electroanalysis* **1997**, *9*, 746-750
37. Niculescu, M. G., S.; Schulte, A.; Csoregi, E.; Schuhmann, W. *Biosensors and Bioelectronics* **2004**, *19*, 1175-1184
38. Walczak, M. M.; Popenoe, D. D.; Deinhammer, R. S.; Lamp, B. D.; Chung, C. K.; Porter, M. D. *Langumir* **1991**, *7*, 2687-2693
39. Widrig, C. A.; Chung, C.; Porter, M. D. *J. Electroanal. Chem.* **1991**, *310*, 335-359
40. Wittstock, G.; Schuhmann, W. *Anal. Chem.* **1997**, *69*, 5059-5066
41. Shiku, H.; Uchida, I.; Matsue, T. *Langumir* **1997**, *13*, 7239 - 7244
42. Wallingford, R. A.; Ewing, A. G. *Anal. Chem.* **1987**, *59*, 1762-1766
43. Osbourn, D. M.; Lunte, C. E. *Analytical Chemistry* **2001**, *73*, 5961-5964
44. Matysik, F. *Electroanalysis* **2000**, *12*, 1349-1355
45. Chen, G.; Ye, J. N.; Cheng, J. S. *Chromatographia* **2000**, *52*, 137-141
46. Wallingford, R. A.; Ewing, A. G. *Analytical Chemistry* **1988**, 1975-1977
47. Holland, L. A.; Lunte, S. M. *Analytical Communications* **1998**, *35*, 1H-4H

48. Sloss, S.; Ewing, A. G. *Anal. Chem.* **1993**, *65*, 577-581
49. O'Shea, T. J.; Lunte, S. M. *Current Separations* **1995**, *14*, 18-25
50. Wallenborg, S. R.; Nyholm, L.; Lunte, C. E. *Anal. Chem.* **1999**, *71*, 544-549
51. Oshea, T. J.; Greenhagen, R. D.; Lunte, S. M. L., C. E.; Smyth, M. R.; Radzik, D. M.; Watanabe, N. *Journal of Chromatography* **1992**, *593*, 305-312
52. Park, S.; McGrath, M. J.; Smyth, M. R.; Diamond, D.; Lunte, C. E. *Anal. Chem.* **1997**, *69*, 2994-3001
53. Whang, C. W.; Chen, I. C. *Anal. Chem.* **1992**, *64*, 2461-2464
54. Olefirowicz, T. M.; Ewing, A. G. *Anal. Chem.* **1990**, *62*, 1872-1876
55. Huang, X.; Zare, R. N.; Sloss, S.; Ewing, A. G. *Anal. Chem.* **1991**, *63*, 189-192
56. Chen, M.; Huang, H. *Analytical Chemistry* **1995**, *67*, 4010-4014
57. Lu, W. Z.; Cassidy, R. M.; Baranski, A. S. *Journal of Chromatography* **1993**, *640*, 433-440
58. Baldwin, R. P.; Ye, J. N. *Anal. Chem.* **1993**, *65*, 3525
59. Matysik, F. M. *Anal. Chem.* **2000**, *72*, 2581
60. Fermier, A. M.; Gostkowski, M. L.; Colon, L. A. *Anal. Chem.* **1996**, *68*, 1661-1664
61. Khaled, M. Y.; Anderson, M. R.; McNair, H. M. *J. Chromatogr. Sci.* **1993**, *31*, 259-264
62. Bard, A. J.; Denuault, G.; Lee, C. M.; Mandler, D.; Wipf, D. O. *Acc. Chem. Res.* **1990**, *23*, 357-363
63. Gatin, M.; Anderson, M. R. *Vibrational Spectroscopy* **1993**, *5*, 255-261
64. Anderson, M. R.; Zhang, M. H. *Langumir* **1994**, *10*, 2807-2813

65. Swalen, J. D.; Allara, D. L.; Andrade, J. D.; Chandross, E. A.; Garoff, S.; Israelachvili, J.; McCarthy, T. J.; Murray, R.; Pease, R. F.; Rabolt, J. F.; Wynne, K. J.; Yu, H. *Langumir* **1987**, *3*, 932-950
66. Imabayashi, S.; Lida, M.; Hobara, D.; Feng, Z. Q.; Niki, K.; Kakiuchi, T. *J. Electroanal. Chem* **1997**, *428*, 33-38
67. Alves, C. A.; Simth, E. L.; Porter, M. D. *Journal of the American Chemical Society* **1992**, *114*, 1222-1227
68. Ulman, A.; Eilers, J. E.; Tillman, N. *Langumir* **1989**, *5*, 1147-1152
69. Finklea, H. O. *Electroanalytical Chemistry: A Series of Advances*, *19*, 109-335
70. Finklea, H. O.; Avery, S.; Lynch, M.; Furtch, T. *Langumir* **1987**, *3*, 409-413
71. Chailapakul, O.; Crooks, R. M. *Langumir* **1993**, *9*, 884-888
72. Nuzzo, R. G.; Dubois, L. H.; Allara, D. L. *Journal of the American Chemical Society* **1990**, *112*, 558-569
73. Sumi, T. U., K. *Journal of Physical Chemistry B* **2004**, *108*, 6422-6428
74. Widrig, G. A.; Chung, C.; Porter, M. D. *Journal of Electroanalytical Chemistry* **1991**, *310*, 335-359
75. Mirkin, C. A.; Zhang, Y.; Salaita, K.; Jung-Hyurk, L. *Nano Letters* **2002**, *2*, 1389-1392
76. Yang, D. F.; Morin, M. *Journal of Electroanalytical Chemistry* **1997**, *429*, 1-5
77. Yang, D. F.; Morin, M. *Journal of Electroanalytical Chemistry* **1998**, *441*, 173-181